Multiuser MIMO Wideband Joint Communications and Sensing System With Subcarrier Allocation

Nhan Thanh Nguyen, *Member, IEEE*, Nir Shlezinger, *Senior Member, IEEE*, Yonina C. Eldar, *Fellow, IEEE*, and Markku Juntti, *Fellow, IEEE*

***Abstract*—In wideband joint communications and sensing (JCAS) systems, the waveforms are often designed and optimized over the entire bandwidth. This significantly limits the degrees of freedom in beamforming and causes severe communications performance loss, especially under a strict radar sensing constraint. In this work, we consider a downlink of a wideband multiuser (MU) multiple-input multiple-output (MIMO) system. We propose a subcarrier allocation strategy incorporated in an efficient JCAS design to improve the communications–sensing performance tradeoff of the system. The main idea is to employ a subset of subcarriers for radar sensing while enabling communications over the entire bandwidth. This creates dedicated subcarriers for communications without any interference from the radar function, whose sensing accuracy can still be guaranteed through strict design constraints. To realize the idea, we formulate the sum rate maximization problem and propose a three-step solution based on successive convex approximation and Riemannian manifold optimization. We further propose efficient initialization methods to reduce complexity and improve the convergence of the employed optimization schemes. Our simulation results for a 32×4 MU-MIMO system show that the proposed scheme offers 70% improvement in the system sum rate while guaranteeing the same radar beampattern mean square error and requiring less radio frequency chains compared with the conventional JCAS design over the entire bandwidth.**

***Index Terms*—Joint communications and sensing, dual-functional radar and communications, hybrid beamforming, wideband, MIMO-OFDM.**

I. Introduction

FUTURE wireless networks are expected to provide very large data rates to support emerging high-speed applications, such as immersive virtual reality, high-definition video, in-room gaming, and intra-large-vehicle communications [1], [2]. To realize such a rapid growth of the data traffic and applications, large bandwidth available at millimeter-wave (mmWave) or Terahertz (THz) bands will be explored [3], [4]. These bands also provide high-range resolutions for radar applications such as target sensing and detection, surveillance, integrated radio frequency (RF) operations, connected automated vehicles [5], [6], and cognitive capabilities [2]. Indeed, wireless communications and radar sensing systems share many commonalities in terms of hardware, signal processing, and network architectures. With further advances in electronics and signal processing, they can be potentially co-located in a joint system [7]. Co-located communications and radar systems are thus the focus of a growing research attention, and have been referred to by various names. These include dual-functional radar communications (DFRC) [8], joint communication and (radar) sensing (JCAS) [9] (which is the term used here), or integrated sensing and communications (ISAC) [10], [11].

Manuscript received 6 April 2023; revised 8 July 2023; accepted 2 August 2013. Date of publication 9 August 2023; date of current version 5 September 2023. This work was supported in part by the Academy of Finland through 6G Flagship under Grant 346208, EERA Project under Grant 332362, Infotech Oulu, Business Finland, Keysight, MediaTek, Siemens, Ekahau, and Verkotan under project 6GLearn. An earlier version of this paper was presented in part at the IEEE Statistical Signal Processing Workshop, 2023. The associate editor coordinating the review of this manuscript and approving it for publication was Dr. Yik-chung Wu. *(Corresponding author: Nhan Thanh Nguyen.)*

Nhan Thanh Nguyen and Markku Juntti are with the Center for Wireless Communications, University of Oulu, FI-90014 Oulu, Finland (e-mail: nhan.nguyen@oulu.fi; markku.juntti@oulu.fi.)

Nir Shlezinger is with the School of ECE, Ben-Gurion University of the Negev, Beer-Sheva 84105, Israel (e-mail: nirshl@bgu.ac.il).

Yonica C. Eldar is with the Faculty of Math and CS, Weizmann Institute of Science, Rehovot 76100, Israel (e-mail: yonina.eldar@weizmann.ac.il.)

Digital Object Identifier 10.1109/TSP.2023.3302622

A. Related Works

Based on the design focuses, current joint communications and radar techniques can be classified into radar-centric, communications-centric, and joint designs [7], [12]. Due to the fast-growing research interest in the topic, radar-centric approaches aim to enhance existing radar technologies such that they can convey messages to remote receivers. This is typically achieved using index modulation techniques on top of conventional radar waveforms [13], [14], [15], or by modulating information the radar sidelobes [16]. These techniques are highly geared towards radar systems, and tend to provide limited throughput [12]. Alternatively, communications-centric designs build on top of communication systems such that they can also sense the environment [17], though typically with limited sensing capabilities. Joint designs provide the flexibility of balancing the contribution of each functionality, and are the focus of this work.

Early studies on the coexistence of communications and radar systems focused on developing interference management approaches to enable smoothly cooperative operations of JCAS systems [18], [19], [20], [21], [22], [23], [24], [25], [26], [27]. A commonly assumed setup considers multiple-input multiple-output (MIMO) techniques due to their spatial beamforming and waveform shaping capabilities via flexible beamforming [28], [29]. Wu et al. [30] proposed a frequency-hopping

MIMO radar-based waveform for channel estimation in JCAS systems. Li et al. [20] proposed spectrum-sharing strategies based on designing transmit covariance matrix to minimize the effective interference power at the radar receiver. In [31], different views of the environment from different users and/or BSs were leveraged to improve sensing performance. More recent studies focus on the design of precoding schemes by formulating overall transmit waveform as the superposition of radar and communications waveforms [24], [25], [26], [27], and on practical constant-modulus waveforms that avoid signal distortion in nonlinear power amplifiers [32], [33], [34], [35], [36]. These works mainly consider conventional small-sized MIMO systems operating at lower and narrow frequency bands such as sub-6GHz and single-carrier systems [16], [22], [32]. This misses two critical aspects of the envisioned JCAS operation, including the usage and degrees of freedom provided by multi-band signaling and the fact that large-scale MIMO systems are likely to involve hybrid beamforming (HBF) architectures.

Multi-band orthogonal frequency division multiplexing (OFDM) MIMO JCAS systems were investigated in [29], [37], [38], [39], [40]. Specifically, Johnston et al. [29] designed radiated waveforms and receive filters for MIMO-OFDM JCAS systems. Wu et al. [37] considered the optimization of OFDM data symbols for a better time and spatial domain signal orthogonality. While both [29] and [37] investigated small-sized MIMO-OFDM JCAS systems, it was shown in [20], [38], [39] that large-scale arrays can significantly reduce the mutual interference between the radar and communications functions. Despite that, the deployment of fully digital beamforming architectures in these systems makes their hardware cost and power consumption prohibitive.

As a solution, HBF architectures require a considerably reduced number of RF chains while maintaining significant beamforming gains [41], [42], [43], [44], [45]. Existing HBF designs in large/massive MIMO JCAS systems were mainly developed for narrowband scenarios [46], [47], [48], [49], [50], based on radar beampattern fitting [46], [47], [48], balancing the signal-to-noise ratios (SNRs) of the two subsystems [49], and minimizing the sensing Cramér-Rao bound [50]. Compared to HBF design for narrowband channels, wideband systems face an extra difficulty. Specifically, in the former, the frequency-independent phase shifters of the standard analog precoder can be optimized for the dedicated frequency-flat channel. However, tuning these analog phase shifters becomes challenging in wideband systems because they must serve multiple frequency-selective channels over the entire frequency band [4], [51], [52], [53]. Cheng et al. [54] and Elbir et al. [55] leveraged model-based [54], [55] and machine learning-based [55] approaches to optimize communications–sensing tradeoff under the power and hardware constraints. Zhang et al. [9] developed a multi-beam technique using a fixed sub-beam for communications and packet-varying scanning sub-beams for sensing. Carneto et al. [56], [57] proposed hybrid beamformers focusing power into sensing directions constraining the power for communications users. Furthermore, beam squint-aware JCAS-HBF designs are considered in [58], [59], [60], where the beam squint effect can be mitigated [58] or exploited [59], [60] properly to improve JCAS operations. The common settings in these wideband JCAS-HBF designs allow operating both communications and sensing over all the sub-bands. This usage limits the degrees of freedom provided by multi-band signaling for JCAS, as discussed next.

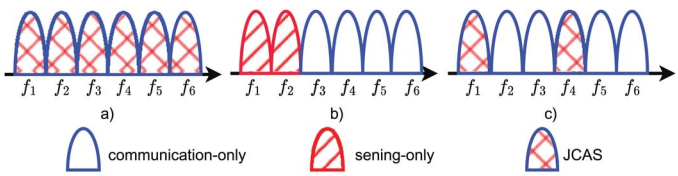

Fig. 1. Subcarrier allocation/sharing approaches: (a) overlapping, (b) non-overlapping, (c) proposed method.

B. Motivations and Contributions

In multicarrier OFDM JCAS systems, subcarrier frequencies can be allocated/shared so that the communications and radar subsystems operate at either overlapping [9], [54], [55], [56], [57], [61], [62] or non-overlapping subcarriers [61], [62], [63], [64], [65], [66], [67]. From the communications perspective, both these subcarrier sharing approaches have their individual limitations. Specifically, in the former, neither the communications beamforming gain nor the sensing accuracy is fully exploited because the overall beampattern needs to serve both communications users and sensing targets simultaneously over the entire bandwidth. In the latter case, the communications performance loss can be significant because the bandwidth fraction allocated for radar cannot be used for data transmission. These difficulties considerably limit the communications–sensing performance tradeoffs in the systems.

To overcome the challenges, we herein propose an efficient JCAS scheme based on monostatic radar sensing by the BS for wideband MIMO-OFDM downlink systems. We unify subcarrier allocation for JCAS and HBF designs. Specifically, we propose allocating a subset of subcarriers for radar sensing, while enabling communications at all available subcarriers; thereby our design can be viewed as communications-centric, which is a common assumption in the evolving 6G systems. With this setting, the communications and radar functionalities are overlapped only at a subset of subcarriers, which are referred to as *JCAS subcarriers*. The BS forms dual-functional (communications-radar) waveforms at the JCAS subcarriers, while it transmits only data signals to communications users via the remaining subcarriers. In this way, both effective sensing and communications can be ensured as long as a proper JCAS subcarrier set is employed with a stricter sensing accuracy constraint. The scheme enables flexible system operation depending on the priorities between the data traffic and the requirements of the sensing service. We illustrate the proposed strategy in comparison with existing ones in Fig. 1.

Relying on this new subcarrier allocation approach, we propose an efficient JCAS design for HBF architectures (JCAS-HBF). Our specific contributions are summarized as follows:

- We first propose a subcarrier allocation strategy, where the communications and sensing functions only interfere with each other within a predetermined subset of subcarriers. This offers additional degrees of freedom for beamforming designs to enhance communications performance.
- We formulate a communications-centric JCAS-HBF design problem as a sum rate maximization constraining on sensing performance, power budget, and constant-modulus analog precoding coefficients. The problem is efficiently solved via a three-step procedure. The proposed scheme allows determining the JCAS subcarriers efficiently with low complexity, while the hybrid precoders are solved via leveraging successive convex approximations (SCA) and Riemannian manifold optimizations. We also propose effective initial solutions to improve the convergence and reduce the overall complexity of the proposed algorithm.
- We analyze the effects of the number of JCAS subcarriers on the communications–sensing performance tradeoff of the considered system. The analysis suggests that fewer JCAS subcarriers but a stricter sensing constraint should be employed to improve the tradeoff. In addition, we find that HBF communications performance can be significantly degraded due to radar sensing, which can also be overcome by using fewer JCAS subcarriers.
- Finally, we present extensive simulation results to demonstrate the superior performance of the proposed subcarrier allocation and JCAS-HBF design. Our results show that despite the reduced number of JCAS subcarriers, the proposed scheme can still generate reliable beampatterns. Particularly, it requires fewer RF chains and offers a significant improvement in communications sum rate while maintaining the same radar sensing accuracy as when performing radar sensing over the entire bandwidth.

C. Paper Organization and Notation

The rest of the paper is organized as follows. Section II presents the signal and channel models and the considered design problems. Section III details the proposed HBF JCAS designs. Numerical results are given in Section V, while Section VI concludes the paper.

Throughout the paper, numbers, vectors, and matrices are denoted by lower-case, boldface lower-case, and boldface upper-case letters, respectively, while $[\mathbf{A}]_{i,j}$ represents the (i,j)-th entry of matrix $\mathbf{A}$. We denote by $(\cdot)^{\mathsf{T}}$ and $(\cdot)^{\mathsf{H}}$ the transpose and the conjugate transpose of a matrix or vector, respectively. The matrix $\mathrm{diag}\{\mathbf{a}_1,\ldots,\mathbf{a}_N\}$ is block diagonal with diagonal columns $\mathbf{a}_1,\ldots,\mathbf{a}_N$. Furthermore, $|\cdot|$ denotes either the absolute value of a scalar or the cardinality of a set, and $\circ$ represents the Hadamard product. We use $\mathcal{CN}(\mu,\sigma^2)$ to denote a complex normal distribution with mean μ and variance σ^2, while $\mathcal{U}[a,b]$ denotes a uniform distribution over given range $[a,b]$.

II. Signal Model and Problem Formulation

A. Signal Model

We consider a MIMO-OFDM JCAS system, where the BS serves as both the radar and communications transmitter. It simultaneously transmits probing signals to the targets and data signals to M single-antenna mobile stations (MSs). Let N denote the number of antennas at the BS, and let $\mathcal{K}=\{1,2,\ldots,K\}$ and $\mathcal{M}=\{1,2,\ldots,M\}$ be the set of subcarriers and MSs, respectively. We assume that while all the subcarriers in $\mathcal{K}$ are used for communications, only a subset $\mathcal{J}\subset\mathcal{K}$ of subcarriers are used for sensing, with $|\mathcal{J}|=J$. Accordingly, the waveforms at subcarriers $k\in\mathcal{J}$ are designed for joint communications with the MSs and sensing the targets, while the remaining subcarriers $k\in\mathcal{K}\backslash\mathcal{J}$ are dedicated to data transmission.

Let $\mathbf{x}[k]\in\mathbb{C}^{N\times 1}$ denote the transmit waveform at subcarrier k. The received signal at MS m is expressed as

$$y_m[k]=\mathbf{h}_m^{\mathsf{H}}[k]\mathbf{x}[k]+n_m[k], \tag{1}$$

where $n_m[k]\sim\mathcal{CN}(0,\sigma_{\mathrm{n}}^2)$ is an additive white Gaussian noise (AWGN) at MS m, and $\mathbf{h}_m[k]\in\mathbb{C}^{N\times 1}$ is the channel vector from the BS to MS m at subcarrier k. Note that unlike the systems considered in [13], [14], [15], [23], [24], [25], [26], [27], the transmit waveform $\mathbf{x}[k]$ in (1) contains only communications data, and the radar waveform is ensured via beamforming design detailed in the next section. This setting allows the communications to be free of interference from the radar subsystem [54], [55].

We adopt the extended Saleh-Valenzuela channel model and express $\mathbf{h}[k]$ as [41]

$$\mathbf{h}[k]=\sum_{p=1}^{P}\alpha_p e^{-j2\pi\tau_p f_k}\mathbf{a}(\phi_p,f_k). \tag{2}$$

In (2), $f_k=f_{\mathrm{c}}+\frac{\mathrm{BW}(k-K)}{2K}$, where BW and f_{c} represent the system bandwidth and center frequency, P is the number of propagation paths, α_p, τ_p, and ϕ_p are the complex gain, time-of-arrival, and angle of departure of the p-th path, respectively. Furthermore, $\mathbf{a}\in\mathbb{C}^{N\times 1}$ denotes the transmit array response vectors. Assuming a uniform linear array (ULA) with half-wavelength antenna spacing, $\mathbf{a}(\phi_p,f_k)$ is given as [41]

$$\mathbf{a}(\phi_p,f_k)=\frac{1}{\sqrt{N}}\left[1,\ldots,e^{j\pi\frac{f_k}{f_{\mathrm{c}}}(N-1)\sin(\phi_p)}\right]^{\mathsf{T}}. \tag{3}$$

We assume that the BS is equipped with a large number of antennas, and thus, it employs HBF using a frequency-flat analog precoder $\mathbf{F}\in\mathbb{C}^{N\times N_{\mathrm{RF}}}$ and frequency-dependent digital baseband precoder $\mathbf{W}[k]\triangleq[\mathbf{w}_1[k],\mathbf{w}_2[k],\ldots,\mathbf{w}_M[k]]\in\mathbb{C}^{N_{\mathrm{RF}}\times M}$. Here, N_{RF} is the number of RF chains at the BS, $M\le N_{\mathrm{RF}}\le N$, and $\mathbf{w}_m[k]$ (i.e., the m-th column of $\mathbf{W}[k]$) represents the digital precoding vectors intended for MS m. We consider the fully-connected HBF architecture implemented with phase shifters. The hybrid precoders satisfy the power constraint $\|\mathbf{FW}[k]\|^2=P_{\mathrm{BS}},\forall k\in\mathcal{K}$, where P_{BS} is the power budget at the BS. Denote by $\mathbf{s}[k]=[s_1[k],s_2[k],\ldots,s_M[k]]\in\mathbb{C}^{M\times 1}$ the transmit symbols at subcarrier k from the BS. Here, we assume that symbol $s_m[k]$ is intended to MS m at subcarrier

k, with $\mathbb{E}\{\mathbf{s}[k]\mathbf{s}[k]^{\mathsf{H}}\} = \mathbf{I}_M$, $k \in \mathcal{K}$. Then, $\mathbf{x}[k] = \mathbf{F}\mathbf{W}[k]\mathbf{s}[k]$ and the signal model in (1) can be rewritten as

$$y_m[k] = \underbrace{\mathbf{h}_m^{\mathsf{H}}[k]\mathbf{F}\mathbf{w}_m[k]s_m[k]}_{\text{desired signal}} + \underbrace{\mathbf{h}_m^{\mathsf{H}}[k]\sum_{j\in\mathcal{M}\setminus m}\mathbf{F}\mathbf{w}_j[k]s_j[k]}_{\text{inter-user interference}} + \underbrace{n_m[k]}_{\text{noise}}. \quad (4)$$

The formulation in (4) captures the dependency of the desired signal and the interference on the subcarrier selection and the HBF setting, motivating the problem formulated in the following subsection.

B. Problem Formulation

To present the problem tackled in the sequel, we first review the radar metric of approaching an ideal beampattern, based on which we formulate the JCAS-HBF design problem.

1) Ideal Radar Beampattern Design: It has been shown in the literature that beampattern design is equivalent to setting the covariance matrix of the probing signals [22]. Therefore, we are interested in designing the covariance matrix of $\bar{\mathbf{R}}[k] \in \mathbb{C}^{N\times N}$ such that the transmit beampattern at subcarrier k, given as $\mathbf{a}^{\mathsf{H}}(\theta_t, f_k)\bar{\mathbf{R}}[k]\mathbf{a}(\theta_t, f_k)$, matches well with a desired beampattern $\mathcal{P}_{\mathrm{d}}(\theta_t, f_k)$ at each angle of elevation $\theta_t \in [-\pi/2, \pi/2]$. Here, $\mathbf{a}(\theta_t, f_k) = \left[1, \ldots, e^{j\pi\frac{f_k}{f_c}(N-1)\sin(\phi_p)}\right]^{\mathsf{T}}$ is the steering vector of the transmit array. Thus, $\bar{\mathbf{R}}[k]$ is designed via minimizing the beampattern mismatch evaluated over a fine angular grid of T angles that covers the detection range $[-\pi/2, \pi/2]$ [22], [32], i.e.,

$$\underset{\{\bar{\mathbf{R}}[k]\}_{k\in\mathcal{J}}}{\text{minimize}} \sum_{k\in\mathcal{J}}\sum_{i=1}^{T}\left|\mathcal{P}_{\mathrm{d}}(\theta_t, f_k) - \mathbf{a}^{\mathsf{H}}(\theta_t, f_k)\bar{\mathbf{R}}[k]\mathbf{a}(\theta_t, f_k)\right| \quad (5a)$$

$$\text{subject to } [\bar{\mathbf{R}}[k]]_{n,n} = \frac{P_{\mathrm{BS}}}{N}, \quad (5b)$$

$$\bar{\mathbf{R}}[k] \succeq \mathbf{0}, \bar{\mathbf{R}}[k] = \bar{\mathbf{R}}^{\mathsf{H}}[k]. \quad (5c)$$

This problem is convex and can be solved by standard convex optimization tools such as CVX.

2) JCAS HBF Design Problem: Based on the signal model in (4), the achievable rate of MS m at subcarrier k is given as

$$r_{mk} = \log_2\left(1 + \frac{|\mathbf{h}_m^{\mathsf{H}}[k]\mathbf{F}\mathbf{w}_m[k]|^2}{\sum_{j\in\mathcal{M}\setminus m}|\mathbf{h}_m^{\mathsf{H}}[k]\mathbf{F}\mathbf{w}_j[k]|^2 + \sigma_{\mathrm{n}}^2}\right). \quad (6)$$

On the other hand, the covariance matrix of the transmit signals vector $\mathbf{x}[k] = \mathbf{F}\mathbf{W}[k]\mathbf{s}[k]$ at the BS at subcarrier k is given as

$$\mathbf{R}[k] = \mathbb{E}\{\mathbf{x}[k]\mathbf{x}^{\mathsf{H}}[k]\} = \mathbf{F}\mathbf{W}[k]\mathbf{W}^{\mathsf{H}}[k]\mathbf{F}^{\mathsf{H}}, \quad (7)$$

where the last equality is due to $\mathbb{E}\{\mathbf{s}[k]\mathbf{s}^{\mathsf{H}}[k]\} = \mathbf{I}_{N_s}, \forall k$. Since the existing literature indicates that the design of the beampattern is equivalent to the design of the covariance matrix of the probing signals [22], [68], the quality of the beampattern formed by the hybrid precoders $\{\mathbf{F}, \mathbf{W}[k]\}$ can be measured by [22], [32], [68]

$$\tau \triangleq \frac{1}{J}\sum_{k\in\mathcal{J}}\left\|\bar{\mathbf{R}}[k] - \mathbf{R}[k]\right\|_{\mathcal{F}}^2 = \frac{1}{J}\sum_{k\in\mathcal{J}}\left\|\bar{\mathbf{R}}[k] - \sum_{m\in\mathcal{M}}\mathbf{F}\mathbf{w}_m[k]\mathbf{w}_m^{\mathsf{H}}[k]\mathbf{F}^{\mathsf{H}}\right\|_{\mathcal{F}}^2. \quad (8)$$

Here, we recall that $\bar{\mathbf{R}}[k]$ is the desired covariance matrix of probing signals for radar sensing, obtained via solving (5) to approach the ideal beampattern. Furthermore, the sensing function is only operated at subcarriers $k \in \mathcal{J}$. Thus, τ reflects the mismatch between the JCAS transmit covariance matrix, formulated in (7) as a function of hybrid precoders $\{\mathbf{F}, \mathbf{W}[k]\}$, and the desired one for the sensing function.

We are interested in designing the JCAS-HBF transceiver to (i) maximize the system per-subcarrier sum rate of all the MSs, given as

$$r = \frac{1}{K}\sum_{k\in\mathcal{K}}\sum_{m\in\mathcal{M}} r_{mk}, \quad (9)$$

and (ii) form beampatterns at subcarriers $k \in \mathcal{J}$ that match well with the desired beampatterns under the transmit power constraint as well as the hardware constraints of analog beamformers. The design is formulated in the following problem:

$$\underset{\mathbf{F},\{\mathbf{W}[k]\},\mathcal{J}}{\text{maximize}}\ r \quad (10a)$$

$$\text{subject to } |[\mathbf{F}]_{i,j}| = 1, \forall i, j, \quad (10b)$$

$$\|\mathbf{F}\mathbf{W}[k]\|^2 = P_{\mathrm{BS}},\ \forall k, \quad (10c)$$

$$\tau \le \tau_0, \quad (10d)$$

$$\mathcal{J} \subset \mathcal{K}, |\mathcal{J}| = J, \quad (10e)$$

where constraint (10b) enforces the modulus of unity for the analog precoding coefficients, (10c) is the power constraint, (10d) is to guarantee the sensing accuracy, and (10e) ensures that only a subset of subcarriers are used for sensing, and the number of JCAS subcarriers is fixed to $J < K$.

We note that (10), even with the fully digital setting (i.e., $N_{\mathrm{RF}} = N$ and $\mathbf{F} = \mathbf{I}_N$), is different from most of the existing JCAS designs in the literature in the following senses. First, its objective is to maximize the communications rate under a required sensing accuracy rather than optimizing the sensing performance under communications SINR constraints as in [22], [32]. This communications-centric design objective is important because, unlike the fully digital systems [22], [32], the communications performance of HBF transceivers is significantly degraded due to the hardware limitations of the analog beamformers. Whereas, when multiple subcarriers are used for radar, the sensing accuracy can be guaranteed even without direct optimization. Second, the optimization of subcarriers set $\mathcal{J}$ in (10) has not been considered in the literature. In this regard, it is interesting that the proposed subcarrier allocation strategy is a generalization of the two conventional subcarrier allocation approaches discussed earlier in Section I-B. Specifically, the overlapping subcarrier sharing can be achieved by setting $\mathcal{J} \equiv \mathcal{K}$, while the non-overlapping method can be designed by (10) with the setting $\tau_0 \approx 0$ in (10d) to force the sensing-only operations at subcarriers $\mathcal{J}$.

Problem (10) is nonconvex and challenging. It inherits the constant-modulus constraints of HBF transceiver design [41], [42], [43] and the strong coupling between the analog and digital precoders, i.e., $\mathbf{F}$ and $\{\mathbf{W}[k]\}$, respectively, in the objective function and constraints (10c), (10d). Furthermore, the design involves integer variables for the JCAS subcarriers in set $\mathcal{J}$. This set is unavailable and to be determined. Thus, it is difficult to address constraint (10d) directly. In the following section, we provide an efficient solution to (10).

III. Proposed JCAS HBF Design

A. General Design Method

Let us denote $\mathbf{q}_m[k] \triangleq \mathbf{F}\mathbf{w}_m[k] \in \mathbb{C}^{N\times 1}, \forall k \in \mathcal{K}$ as the effective precoding vector intended for MS m at subcarrier k. We can rewrite τ in (8) and r_{mk} in (9) as

$$\tilde{\tau} = \frac{1}{J}\sum_{k\in\mathcal{J}}\left\|\bar{\mathbf{R}}[k] - \sum_{m\in\mathcal{M}}\mathbf{q}_m[k]\mathbf{q}_m^{\mathsf{H}}[k]\right\|_{\mathcal{F}}^2, \tag{11}$$

$$\tilde{r}_{mk} = \log_2\left(1 + \frac{\left|\mathbf{h}_m^{\mathsf{H}}[k]\mathbf{q}_m[k]\right|^2}{\sum\limits_{j\in\mathcal{M}\backslash m}\left|\mathbf{h}_m^{\mathsf{H}}[k]\mathbf{q}_j[k]\right|^2 + \sigma_{\mathrm{n}}^2}\right), \tag{12}$$

respectively. As a result, problem (10) can be rewritten as

$$\underset{\{\mathbf{q}_m[k]\},\mathcal{J}}{\text{maximize}} \quad \frac{1}{K}\sum_{k\in\mathcal{K}}\sum_{m\in\mathcal{M}}\tilde{r}_{mk} \tag{13a}$$

$$\text{subject to} \quad \sum_{m\in\mathcal{M}}\left\|\mathbf{q}_m[k]\right\|^2 = P_{\mathrm{BS}}, \forall k, \tag{13b}$$

$$\tilde{\tau} \le \tau_0. \tag{13c}$$

The introduction of $\{\mathbf{q}_m[k]\}$ significantly simplifies the problem as the constant modulus constraint has been relaxed [58], [69]. However, the difficulty involved with $\mathcal{J}$ remains. To tackle this, we exploit the observation in (13) that the sensing constraint (13c) does not depend on channels $\{\mathbf{h}_m[k]\}, k \in \mathcal{K}\backslash\mathcal{J}$. This implies that

- For any set $\mathcal{J}$, the effective precoders $\{\mathbf{q}_m[k]\}$ can be designed to maximize the objective function over the set $\mathcal{K}\backslash\mathcal{J}$, i.e., $\sum_{k\in\mathcal{K}\backslash\mathcal{J}}\sum_{m\in\mathcal{M}}\tilde{r}_{mk}$, without affecting the sensing performance.
- Given $\{\mathbf{q}_m[k]\}$, if $\mathcal{J}$ contains subcarriers $\{k\}$ that minimizes $\tilde{\tau}$ in (11), it offers the best sensing performance. Another important benefit of choosing such $\mathcal{J}$ is that the minimal $\tilde{\tau}$ improves the chance that constraint (13c) is satisfied, leading to a larger feasible space for a larger objective in (13a). Thus, it improves the communications performance at the same time.

The above observations motivate the procedure outlined in Algorithm 1 to solve (10). In this algorithm, all the effective precoders $\{\mathbf{q}_m[k]\}, \forall k$ are first designed for sum rate maximization in (14). With given $\{\mathbf{q}_m[k]\}, \forall k$, $\mathcal{J}$ is chosen as the set of subcarriers that offer the smallest $\tilde{\tau}$. Then, $\{\mathbf{q}_m[k]\}, k \in \mathcal{J}$ are refined in (15) to consider the sensing design. Finally, the analog and digital precoders, i.e., $\mathbf{F}, \{\mathbf{w}_m[k]\}$, are obtained by factorizing $\{\mathbf{q}_m[k]\}$ in (16). We note that in (15), the sensing constraint (13c) is integrated into the objective function as a penalty term with a weighting factor ρ. This simplifies the design because, on the one hand, the feasible region is expanded to improve the feasibility probability [22], on the other hand, the weighted objective function in (15a) motivates a manifold optimization-based solution. However, this transformation does not reduce the design efficiency because a better sensing performance (corresponding to a smaller τ_0 in (13c)) can be achieved by a larger ρ. Indeed, for given $\bar{\mathbf{q}}[k]$ and $\bar{\mathbf{R}}[k]$, increasing ρ enhance the contribution of the sensing metric while reducing that of the communications metric to the overall objective function (15a) (as $\bar{\rho} = 1 - \rho$). In this case, the design in (15) tends to minimize the sensing covariance mismatch in the first term of (15a), leading to improved sensing performance. We will further numerically justify this in Section V.

The proposed procedure applies to both the designs of fully-digital beamforming (DBF) and HBF. Specifically, for the former, the digital precoders can be obtained by the first three steps in Algorithm 1, while the last step is additionally required to obtain the hybrid precoders in the HBF problem. Subproblems (14)–(16) are nonconvex. However, their structures motivate efficient solutions via SCA and Riemannian manifold optimization, as detailed next.

Algorithm 1 Overall JCAS-HBF Design

Require: $\{\mathbf{h}_m[k]\}$.
Ensure: $\mathbf{F}, \{\mathbf{W}[k]\}$.

1: Solve the sum rate maximization problem without sensing constraint, i.e.,

$$\underset{\{\mathbf{q}_m[k]\}}{\text{maximize}} \quad \frac{1}{K}\sum_{k\in\mathcal{K}}\sum_{m\in\mathcal{M}}\tilde{r}_{mk} \tag{14a}$$

$$\text{subject to} \quad (13b) \tag{14b}$$

to obtain solutions $\{\hat{\mathbf{q}}_m[k]\}, k \in \mathcal{K}$.

2: Compute $\{\tilde{\tau}_1, \ldots, \tilde{\tau}_K\}$, $\tilde{\tau}_k = \left\|\bar{\mathbf{R}}[k] - \sum_{m\in\mathcal{M}}\hat{\mathbf{q}}_m[k]\hat{\mathbf{q}}_m^{\mathsf{H}}[k]\right\|_{\mathcal{F}}^2$. Obtain set $\mathcal{J}$ containing the J indices of the J smallest values in $\{\tilde{\tau}_1, \ldots, \tilde{\tau}_K\}$.

3: Solve the JCAS problem

$$\underset{\{\mathbf{q}_m[k]\}}{\text{minimize}} \quad \frac{\rho}{J}\sum_{k\in\mathcal{J}}\left\|\sum_{m\in\mathcal{M}}\mathbf{q}_m[k]\mathbf{q}_m^{\mathsf{H}}[k] - \bar{\mathbf{R}}[k]\right\|_{\mathcal{F}}^2 + \frac{\bar{\rho}}{J}\sum_{k\in\mathcal{J}}\sum_{m\in\mathcal{M}}\left\|\mathbf{q}_m[k] - \hat{\mathbf{q}}_m[k]\right\|^2 \tag{15a}$$

$$\text{subject to} \quad (13b) \tag{15b}$$

to obtain $\{\tilde{\mathbf{q}}_m[k]\}, k \in \mathcal{J}$, where ρ is the weighting factor balancing the communications and sensing performance, and $\bar{\rho} \triangleq 1 - \rho$.

4: Obtain hybrid precoders $\mathbf{F}$ and $\{\mathbf{w}_m[k]\}$ by solving the constrained least squares (LS) problem

$$\underset{\{\mathbf{F},\mathbf{w}_m[k]\}}{\text{minimize}} \quad \sum_{k\in\mathcal{K}}\sum_{m\in\mathcal{M}}\left\|\bar{\mathbf{q}}_m[k] - \mathbf{F}\mathbf{w}_m[k]\right\|^2 \tag{16a}$$

$$\text{subject to} \quad (10b), (10c), \tag{16b}$$

where

$$\bar{\mathbf{q}}_m[k] = \begin{cases}\tilde{\mathbf{q}}_m[k], & k \in \mathcal{J}\\ \hat{\mathbf{q}}_m[k], & \text{otherwise.}\end{cases} \tag{17}$$

B. Detailed Solutions to Problems (14)–(16)

1) Solution to Problem (14):

Linear Zero-Forcing Solution: We first consider zero-forcing (ZF) beamforming with power allocation as the low-complexity solution to the effective precoder, which manages the inter-user interference. The ZF precoder is given as

$$\mathbf{Q}_{\text{ZF}}[k] = \mathbf{H}^{\dagger}[k]\mathbf{P}^{\frac{1}{2}}[k], \tag{18}$$

where $\mathbf{H}[k] \triangleq [\mathbf{h}_1[k], \ldots, \mathbf{h}_M[k]]^{\mathsf{H}}$, $\mathbf{H}^{\dagger}[k] = \mathbf{H}^{\mathsf{H}}[k]\left(\mathbf{H}[k]\mathbf{H}^{\mathsf{H}}[k]\right)^{-1}$, and $\mathbf{P}[k] = \text{diag}\left\{p_1[k], \ldots, p_M[k]\right\}$ is determined by water-filling method. Specifically, $p_m[k]$ is the water-filling power factor associated with MS m and subcarrier k, given as

$$p_m[k] = \max\left\{\frac{1}{\mu[k]} - \|\breve{\mathbf{h}}_m[k]\|^2\sigma_{\text{n}}^2, 0\right\}, \tag{19}$$

where $\mu[k]$ is chosen such that $\sum_{m\in\mathcal{M}} p_m[k] = P_{\text{BS}}$ and $\breve{\mathbf{h}}_m[k]$ is the m column of $\mathbf{H}^{\dagger}[k]$.

Iterative SCA Solution: The ZF solution has low complexity but is suboptimal. We herein propose an iterative solution to attain improved effective precoders via SCA. Specifically, let us denote

$$\mathbf{q}[k] \triangleq [\mathbf{q}_1^{\mathsf{T}}[k], \ldots, \mathbf{q}_M^{\mathsf{T}}[k]]^{\mathsf{T}}, \tag{20}$$

$$\tilde{\mathbf{G}}_m[k] \triangleq \mathbf{h}_m[k]\mathbf{h}_m^{\mathsf{H}}[k], \tag{21}$$

$$\hat{\mathbf{G}}_m[k] \triangleq \text{blkdiag}\{\underbrace{\mathbf{0}, \ldots, \mathbf{0}}_{m-1 \text{ terms}}, \tilde{\mathbf{G}}_m[k], \underbrace{\mathbf{0}, \ldots, \mathbf{0}}_{M-m \text{ terms}}\}, \tag{22}$$

$$\bar{\mathbf{G}}_m[k] \triangleq \text{blkdiag}\{\underbrace{\tilde{\mathbf{G}}_m[k], \ldots, \tilde{\mathbf{G}}_m[k]}_{m-1 \text{ terms}}, \mathbf{0}, \underbrace{\tilde{\mathbf{G}}_m[k], \ldots, \tilde{\mathbf{G}}_m[k]}_{M-m \text{ terms}}\}, \tag{23}$$

which have sizes $NM \times 1, N \times N, NM \times NM$, and $NM \times NM$, respectively. Furthermore, we introduce slack variables $\{\zeta_m[k]\}$ as the lower bound of the SINR terms in (12). Then, the hybrid precoder design in (14) can be reformulated as

$$\underset{\{\mathbf{q}[k],\zeta_m[k]\}}{\text{maximize}} \ \frac{1}{K}\sum_{k\in\mathcal{K}}\sum_{m\in\mathcal{M}} \log_2\left(1+\zeta_m[k]\right) \tag{24a}$$

$$\text{subject to} \ \frac{\mathbf{q}^{\mathsf{H}}[k]\hat{\mathbf{G}}_m[k]\mathbf{q}[k]}{\mathbf{q}^{\mathsf{H}}[k]\bar{\mathbf{G}}_m[k]\mathbf{q}[k]+\sigma_{\text{n}}^2} \geq \zeta_m[k], \ \forall m,k, \tag{24b}$$

$$\|\mathbf{q}[k]\|^2 \leq P_{\text{BS}}, \ \forall k, \tag{24c}$$

where we have relaxed the power constraint in (24c); however, constraint (24b) is still nonconvex. We tackle this constraint by rewriting it as

$$\mathbf{q}^{\mathsf{H}}[k]\bar{\mathbf{G}}_m[k]\mathbf{q}[k] + \sigma_{\text{n}}^2 \leq f_{\texttt{qol}}(\mathbf{q}[k], \zeta_m[k]), \ \forall m,k, \tag{25}$$

where $f_{\texttt{qol}}(\mathbf{q}[k], \zeta_m[k]) \triangleq \frac{\mathbf{q}^{\mathsf{H}}[k]\hat{\mathbf{G}}_m[k]\mathbf{q}[k]}{\zeta_m[k]}$ is a quadratic-over-linear function. Based on the first-order Taylor approximation around feasible point $(\mathbf{q}[k]_i, \zeta_m[k]_i)$, an upper bound of $f_{\texttt{qol}}(\mathbf{q}[k], \zeta_m[k])$ in (25) can be found as

$$f_{\texttt{qol}}(\mathbf{q}[k], \zeta_m[k]) \leq F_{\texttt{qol}}(\mathbf{q}[k], \zeta_m[k]; \mathbf{q}[k]_i, \zeta_m[k]_i), \ \forall m,k, \tag{26}$$

Algorithm 2 Solving Problem (14) via SCA.

Require: $\{\mathbf{h}_m[k]\}$.
Ensure: $\bar{\mathbf{q}}_m[k]$.
1: Obtain $\tilde{\mathbf{G}}_m[k]$, $\hat{\mathbf{G}}_m[k]$, and $\bar{\mathbf{G}}_m[k], \forall m,k$ based on (21)–(23), respectively.
2: Set $i=0$. Initialize $\mathbf{q}_m[k]_0 = \text{vec}\left(\mathbf{Q}_{\text{ZF}}[k]\right)$, where $\mathbf{Q}_{\text{ZF}}[k]$ is obtained as in (18). Set $\zeta_m[k]_0$ for the equality in (24b).
3: **repeat**
4: Solve problem (29) for given $\mathbf{q}[k]_i$ and $\zeta_m[k]_i$ to obtain $\mathbf{q}[k]^{\star}$ and $\zeta_m[k]^{\star}$.
5: Update $\mathbf{q}[k]_{i+1} = \mathbf{q}[k]^{\star}$ and $\zeta_m[k]_{i+1} = \zeta_m[k]^{\star}$.
6: Set $i = i+1$.
7: **until** convergence
8: Return $\{\hat{\mathbf{q}}_m[k]\}$ as $\{\mathbf{q}[k]^{\star}\}$ at convergence, $\forall k$.

where

$$F_{\texttt{qol}}(\mathbf{q}[k], \zeta_m[k]; \mathbf{q}[k]_i, \zeta_m[k]_i) \triangleq \frac{\mathbf{q}^{\mathsf{H}}[k]_i\hat{\mathbf{G}}_m[k]\mathbf{q}[k]_i}{\left(\zeta_m[k]_i\right)^2}\zeta_m[k] - \frac{2\Re\left(\mathbf{q}^{\mathsf{H}}[k]_i\hat{\mathbf{G}}_m[k]\mathbf{q}[k]\right)}{\zeta_m[k]_i}. \tag{27}$$

Thus, constraint (24b) can be approximated in the i-th iteration by the following convex one:

$$\mathbf{q}^{\mathsf{H}}[k]\bar{\mathbf{G}}_m[k]\mathbf{q}[k] + \sigma_{\text{n}}^2 \leq F_{\texttt{qol}}(\mathbf{q}[k], \zeta_m[k]; \mathbf{q}[k]_i, \zeta_m[k]_i), \ \forall m,k. \tag{28}$$

As a result, problem (24) is approximated by the following convex problem in iteration i:

$$\underset{\{\mathbf{q}[k],\zeta_m[k]\}}{\text{maximize}} \ \frac{1}{K}\sum_{k\in\mathcal{K}}\sum_{m\in\mathcal{M}} \log_2\left(1+\zeta_m[k]\right) \tag{29a}$$

$$\text{subject to} \ (28), (24c), \tag{29b}$$

which can be solved via standard convex optimization tools such as CVX and MOSEK.

The iterative procedure to solve problem (14) is summarized in Algorithm 2. We employ the low-complexity ZF solution in (18) to initialize $\mathbf{q}_m[k]_0$, which will be shown via simulations to significantly accelerate the convergence of this algorithm. Accordingly, $\zeta_m[k]_0$ is set to the SINR in the left-hand-side (LHS) of (24b) at $\mathbf{q}_m[k]_0$. In each iteration, the solutions to $\mathbf{q}[k]$ and $\zeta_m[k]$ are updated until a convergence criterion is satisfied. The solution at the convergence of this algorithm is defined as $\{\hat{\mathbf{q}}_m[k]\}$ and is leveraged next.

2) Solution to Problem (15): Let us denote

$$\mathbf{Q}[k] \triangleq [\mathbf{q}_1[k], \ldots, \mathbf{q}_M[k]] \in \mathbb{C}^{N\times M}, \tag{30}$$

$$\hat{\mathbf{Q}}[k] \triangleq [\hat{\mathbf{q}}_1[k], \ldots, \hat{\mathbf{q}}_M[k]] \in \mathbb{C}^{N\times M}. \tag{31}$$

Then, we can rewrite problem (15) as

$$\underset{\{\mathbf{Q}[k]\}}{\text{minimize}} \ \gamma \triangleq \frac{1}{J}\sum_{k\in\mathcal{J}}\gamma_k \tag{32a}$$

$$\text{subject to} \ \|\mathbf{Q}[k]\|_{\mathcal{F}}^2 = P_{\text{BS}}, \forall k \in \mathcal{J}, \tag{32b}$$

where

$$\gamma_k \triangleq \rho\left\|\mathbf{Q}[k]\mathbf{Q}^{\mathsf{H}}[k] - \bar{\mathbf{R}}[k]\right\|_{\mathcal{F}}^2 + \bar{\rho}\left\|\mathbf{Q}[k] - \hat{\mathbf{Q}}[k]\right\|_{\mathcal{F}}^2. \tag{33}$$

It is observed that the constraints (32b) are independent across $k \in \mathcal{J}$. Therefore, this problem can be solved across k independently, i.e.,

$$\underset{\mathbf{Q}[k]\in\mathscr{Q}}{\text{minimize}} \quad \gamma_k, \tag{34}$$

where $\mathscr{Q} \triangleq \{\mathbf{Q}[k] \in \mathbb{C}^{N\times M} : \|\mathbf{Q}[k]\|_{\mathcal{F}} = \sqrt{P_{\text{BS}}}\}$ is the complex hypershpere manifold with radius $\sqrt{P_{\text{BS}}}$. This motivates a Riemannian manifold minimization approach [41] to efficiently find the near-optimal solution to (34). Next, we present the results on the Euclidean and Riemannian gradients of γ_k, which are required to update $\mathbf{Q}[k]$ over iterations of Riemannian manifold minimization. For the detailed concepts in the approach, we refer readers to [22].

First, the Euclidean of γ_k is computed as

$$\nabla\gamma_k = 4\rho\left(\mathbf{Q}[k]\mathbf{Q}^{\text{H}}[k] - \bar{\mathbf{R}}[k]\right)\mathbf{Q}[k] + 2\bar{\rho}\left(\mathbf{Q}[k] - \hat{\mathbf{Q}}[k]\right). \tag{35}$$

A tangent space corresponds to the complex hypersphere $\mathscr{Q}$ is given by

$$T_{\mathbf{Q}[k]}\mathscr{Q} = \left\{\mathbf{Q}[k] \in \mathbb{C}^{N\times M} : \Re(\text{trace}\left(\mathbf{Q}^{\text{H}}[k]\mathbf{Q}[k]\right)) = 0\right\},$$

where $\Re(\cdot)$ denotes the real part of a complex number. The Riemannian gradient corresponding to the Euclidean $\nabla\gamma_k$, denoted as $\text{grad}\gamma_k$, is obtained by projecting $\nabla\gamma_k$ onto tangent space $T_{\mathbf{Q}[k]}\mathscr{Q}$:

$$\begin{aligned}\text{grad}\gamma_k &= \text{proj}_{\mathbf{Q}[k]}\left(\nabla\gamma_k\right)\\ &= \nabla\gamma_k - \Re(\text{trace}\left(\mathbf{Q}^{\text{H}}[k]\nabla\gamma_k\right))\mathbf{Q}[k].\end{aligned} \tag{36}$$

In an iteration of the Riemannian conjugate gradient scheme, say iteration $i+1$, $\mathbf{Q}[k]$ is updated and projected back onto the manifold by a retraction, i.e.,

$$\mathbf{Q}[k]_{i+1} = \frac{\sqrt{P_{\text{BS}}}\left(\mathbf{Q}[k]_i + \delta_i\mathbf{\Pi}_i\right)}{\|\mathbf{Q}[k]_i + \delta_i\mathbf{\Pi}_i\|_{\mathcal{F}}}. \tag{37}$$

where δ_i is the Armijo backtracking line search step size, and $\mathbf{\Pi}_i$ is the descent direction,

$$\mathbf{\Pi}_i = -\text{grad}\gamma_{k,i} + \mu_i\mathcal{T}_{i-1\to i}\left(\mathbf{\Pi}_{i-1}\right), \tag{38}$$

Here, $\text{grad}\gamma_{k,i}$ is the Riemannian gradient $\text{grad}\gamma_k$ at $\mathbf{Q}[k] = \mathbf{Q}[k]_i$, and $\mathcal{T}_{i-1\to i}\left(\mathbf{\Pi}_{i-1}\right)$ transports $\mathbf{\Pi}_{i-1}$ from tangent space $T_{\mathbf{Q}[k]_{i-1}}\mathscr{Q}$ to tangent space $T_{\mathbf{Q}[k]_i}\mathscr{Q}$, specified as

$$\mathcal{T}_{i-1\to i}\left(\mathbf{\Pi}_{i-1}\right) = \mathbf{\Pi}_{i-1} - \Re(\text{trace}\left(\mathbf{Q}^{\text{H}}[k]_i\mathbf{\Pi}_{i-1}\right))\mathbf{Q}[k]_i.$$

In (38), μ_i is a Polak-Ribiere parameter which is computed as

$$\mu_i = \frac{\langle\text{grad}\gamma_{k,i}, \overline{\text{grad}}\gamma_{k,i}\rangle}{\langle\text{grad}\gamma_{k,i-1}, \text{grad}\gamma_{k,i-1}\rangle}, \tag{39}$$

where $\langle\mathbf{X},\mathbf{Y}\rangle \triangleq \Re(\text{trace}\left(\mathbf{X}^{\text{H}}\mathbf{Y}\right))$ denotes the usual Euclidean inner product, and $\overline{\text{grad}}\gamma_{k,i} = \text{grad}\gamma_{k,i} - \mathcal{T}_{i-1\to i}\left(\text{grad}\gamma_{k,i-1}\right)$.

Algorithm 3 summarizes the steps to solve problem (15). Specifically, $\hat{\mathbf{Q}}[k]$ is first obtained based on (31), and then, the initial solution to $\mathbf{Q}[k]_0$ is set. Next, $\mathbf{Q}[k]_i$ is updated over iterations in steps 4–10 until convergence. Here, we recall that in this algorithm, only the effective precoders at subcarriers $k \in \mathcal{J}$ are solved. The solutions at convergence, i.e., $\{\tilde{\mathbf{q}}_m[k]\}, k \in \mathcal{J}$ will be used to find the final hybrid precoders as detailed next.

Algorithm 3 Riemannian Manifold Solution to Problem (15)

Require: $\mathcal{J}, \{\bar{\mathbf{R}}[k], \hat{\mathbf{q}}_m[k]\}, \forall k \in \mathcal{J}$.
Ensure: $\tilde{\mathbf{q}}_m[k], \forall k \in \mathcal{J}$.
1: **for** $k \in \mathcal{J}$ **do**
2: Obtain $\hat{\mathbf{Q}}[k]$ based on (31).
3: Set $i = 0$, randomly initialize $\mathbf{Q}[k]_0 \in \mathscr{Q}$ and set $\mathbf{\Pi}_0 = -\text{grad}\gamma_{k,0}$.
4: **repeat**
5: Obtain step size δ_i by Armijo rule.
6: Update $\mathbf{Q}[k]_{i+1}$ based on (37).
7: Compute μ_{i+1} based on (39).
8: Compute $\mathbf{\Pi}_{i+1}$ based on (38).
9: $i = i + 1$.
10: **until** convergence
11: Return $\{\tilde{\mathbf{q}}_m[k]\}, k \in \mathcal{J}$ as the columns of $\{\mathbf{Q}[k]\}, k \in \mathcal{J}$ at convergence.
12: **end for**

3) Solution to Problem (16): By letting

$$\bar{\mathbf{Q}}[k] \triangleq [\bar{\mathbf{q}}_1[k], \ldots, \bar{\mathbf{q}}_M[k]] \in \mathbb{C}^{N\times M}. \tag{40}$$

where $\bar{\mathbf{q}}_m[k]$ is defined as (17), we can rewrite problem (16) as

$$\underset{\{\mathbf{F},\mathbf{W}[k]\}}{\text{minimize}}\ \eta \triangleq \sum_{k\in\mathcal{K}}\left\|\bar{\mathbf{Q}}[k] - \mathbf{F}\mathbf{W}[k]\right\|_{\mathcal{F}}^2 \tag{41a}$$

$$\text{subject to } (10\text{b}), (10\text{c}). \tag{41b}$$

This is a matrix factorization problem, which requires factorizing matrix $\bar{\mathbf{Q}}[k]$ into analog and digital precoding matrices $\mathbf{F}$ and $\mathbf{W}[k]$. We herein apply the alternating minimization framework, in cooperation with LS solution and Riemannian manifold optimization [41], to find the near-optimal solution to (41). Specifically, in the i-th iteration of the alternating procedure, $\mathbf{W}[k]_i$ depends on $\mathbf{F}_i$ in the following normalized LS solution:

$$\mathbf{W}[k]_i = \sqrt{P_{\text{BS}}}\frac{\mathbf{F}_i^{\dagger}\bar{\mathbf{Q}}[k]}{\|\mathbf{F}_i^{\dagger}\bar{\mathbf{Q}}[k]\|_{\mathcal{F}}}. \tag{42}$$

which satisfies the power constraint (10c). Thus, the remained task is to solve $\mathbf{F}$ with given $\{\mathbf{W}[k]\}$. Let us denote

$$\mathbf{f} \triangleq \text{vec}(\mathbf{F}) \in \mathbb{C}^{NN_{\text{RF}}\times 1}, \tag{43}$$

$$\mathbf{z}[k] \triangleq \text{vec}(\mathbf{Q}[k]) \in \mathbb{C}^{NM\times 1}, \tag{44}$$

$$\mathbf{V}[k] \triangleq \mathbf{W}^{\text{T}}[k] \otimes \mathbf{I}_{N_{\text{t}}} \in \mathbb{C}^{NN_{\text{RF}}\times NM}. \tag{45}$$

Then, $\mathbf{f}$ is the solution to the following problem:

$$\underset{\mathbf{f}\in\mathscr{F}}{\text{minimize}}\ \eta = \sum_{k\in\mathcal{K}}\|\mathbf{z}[k] - \mathbf{V}[k]\mathbf{f}\|^2 \tag{46}$$

where $\mathscr{F} \triangleq \{\mathbf{f} \in \mathbb{C}^{NN_{\text{RF}}\times 1} : |f_n| = 1, n = 1, \ldots, NN_{\text{RF}}\}$ is the feasible set of $\mathbf{f}$, where f_n represents the n-th element of $\mathbf{f}$. Here, $\mathscr{F}$ is a complex circle manifold with the corresponding tangent space $T_{\mathbf{f}}\mathscr{F} = \left\{\mathbf{f} \in \mathbb{C}^{NN_{\text{RF}}\times 1} : \Re(\mathbf{f}\circ\mathbf{f}^*) = \mathbf{0}_{NN_{\text{RF}}}\right\}$, where $\mathbf{0}_{NN_{\text{RF}}}$ represents the vector of NN_{RF} zeros. This problem can be solved similarly as Algorithm 3. Hence, we omit the detailed derivations and only present key results on the gradients, retraction, and vector transport to apply Algorithm 3. They are respectively given as:

$$\nabla\eta = -2\sum_{k\in\mathcal{K}}\mathbf{V}^{\text{H}}[k](\mathbf{z}[k] - \mathbf{V}[k]\mathbf{f}), \tag{47}$$

Algorithm 4 Alternating Minimization for Problem (16)

Require: $\bar{\mathbf{q}}_m[k], \forall k$.
Ensure: $\mathbf{F}, \mathbf{W}[k], \forall k$.
1: Obtain $\bar{\mathbf{Q}}[k]$ based on (40).
2: Set $i = 0$. Initialize $\mathbf{F}_0$ based on (52) and obtain $\mathbf{W}[k]_0$ based on (42).
3: **repeat**
4: Apply Riemannian manifold approach to obtain $\mathbf{f}_{i+1}$ based on updating (47)–(51) until convergence.
5: Reconstruct $\mathbf{F}_{i+1}$ from $\mathbf{f}_{i+1}$ and obtain $\mathbf{W}[k]_{i+1}$ based on (42).
6: $i = i + 1$.
7: **until** convergence
8: Return $\mathbf{F}$ and $\{\mathbf{W}[k]\}$.

$$\text{grad}\eta_i = \nabla\eta_i - \Re(\nabla\eta_i \circ \mathbf{f}_i^*) \circ \mathbf{f}_i, \tag{48}$$

$$\mathcal{T}_{i-1\to i}(\boldsymbol{\pi}_{i-1}) = \Re\big(\boldsymbol{\pi}_{i-1} \circ \mathbf{f}_{i+1}^*\big) \circ \mathbf{f}_{i+1}, \tag{49}$$

$$\boldsymbol{\pi}_i = -\text{grad}\eta_i + \mu_i\Big[\boldsymbol{\pi}_{i-1} - \mathcal{T}_{i-1\to i}(\boldsymbol{\pi}_{i-1})\Big], \tag{50}$$

$$\mathbf{f}_{i+1} = \frac{\mathbf{f}_i + \delta_i\boldsymbol{\pi}_i}{|\mathbf{f}_i + \delta_i\boldsymbol{\pi}_i|}. \tag{51}$$

Based on (47)–(51), the alternating minimization solving problem (16) is summarized in Algorithm 4. We note that step 4 in this algorithm is an iterative procedure, similar to steps 4–10 of Algorithm 3. Thus, Algorithm 4 requires a nested loop, which causes slow convergence and potentially high computational complexity. To overcome this, we propose initializing the RF precoder $\mathbf{F}_0$ as:

$$[\mathbf{F}_0]_{i,j} = e^{\angle[\mathbf{U}]_{i,j}}, \tag{52}$$

where $\mathbf{U} \in \mathbb{C}^{N\times N_{\text{RF}}}$ is taken from N_{RF} eigenvectors of $\bar{\mathbf{Q}}[c]\bar{\mathbf{Q}}[c]^{\text{H}}$ with c implying the center subcarrier, and $\angle[\mathbf{U}]_{i,j}$ represents the phase of the (i,j)-th entry of $\mathbf{U}$. This initialization approach is based on the analog precoding scheme in [70]. However, instead of using the matrix $[\bar{\mathbf{Q}}[1],\ldots,\bar{\mathbf{Q}}[K]]$ [70], we found that utilizing $\bar{\mathbf{Q}}[c]$ yields a better initial point and faster convergence. Furthermore, it is clear that initializing with $\bar{\mathbf{Q}}[c] \in \mathbb{C}^{N\times M}$ is also much more computationally efficient than doing that with $[\bar{\mathbf{Q}}[1],\ldots,\bar{\mathbf{Q}}[K]] \in \mathbb{C}^{N\times MK}$.

C. Complexity and Convergence Analysis

We end this section with a complexity and convergence analysis of our JCAS-HBF design in Algorithm 1, with specific solutions being presented in Algorithms 2–4.

Algorithm 2 solves $MNK + MK$ variables and $MK + K$ constraints in each iteration. Thus, it requires a complexity of $\mathcal{I}_2\mathcal{O}\left(((M+1)K)^{\frac{1}{2}}(N+1)^3M^3K^3\right)$, where $\mathcal{I}_2$ is the number of iterations until convergence of Algorithm 2. Here, we ignore the complexity for initialization with the linear ZF solution (18) because it is much lower than the complexity required for the updates inside the iterations, i.e., steps 3–7. We note that problem (14) can be solved via semidefinite relaxation (SDR) approach [26] by solving the effective transmit covariance matrix rather than effective precoders. However, this will cost a complexity of approximately $\mathcal{O}\left(M^{6.5}K^{6.5}\right)$ [26] and require a Gaussian approximation to reconstruct the effective precoders.

Let $r(\{\mathbf{q}[k]_i, \zeta_m[k]_i\})$ be the objective values of problem (29) obtained in the i-th iteration of Algorithm 2. In the $(i+1)$-th iteration, $\{\mathbf{q}[k]_i, \zeta_m[k]_i\}$ is a feasible point of (29). Thus, its corresponding objective value, i.e., $r(\{\mathbf{q}[k]_i, \zeta_m[k]_i\})$, cannot be larger than the optimal value of (29), i.e.,

$$r(\{\mathbf{q}[k]_{i+1}, \zeta_m[k]_{i+1}\}) \geq r(\{\mathbf{q}[k]_i, \zeta_m[k]_i\}). \tag{53}$$

As a result, Algorithm 2 returns non-decreasing objective values over iterations. Furthermore, the objective function is a monotonically increasing function of the SINR terms $\{\zeta_m[k]\}$, which are upper bounded by constraints (28) and (24c), in turn implying that $r(\cdot)$ is also upper bounded. Accordingly, convergence of Algorithm 2 is guaranteed by the monotone convergence theorem [71, Theorem 3.14].

In each iteration, Algorithm 3 performs a line search to obtain the step size δ_i and a retraction to update $\mathbf{Q}[k]_{i+1}$. Furthermore, it computes the Euclidean gradient to update the direction, which is then used for computing the vector transports. Among these steps, the complexity to compute the Euclidean gradient in (35) is the highest and dominates the others [22]. Thus, the overall complexity of Algorithm 3 can be approximated as $\mathcal{I}_3 J\mathcal{O}\left(4N^2M + 3N\right)$, with $\mathcal{I}_3$ being the number of iterations in Algorithm 3. It is observed that the overall complexity of this algorithm is proportional to J. To the best knowledge of the authors, the convergence Riemannian manifold optimization remains an open problem. Thus, it is rather difficult to analyze the convergence of Algorithm 3.

Finally, we analyze the complexity of Algorithm 4. It is observed from (45) that $\mathbf{V}[k]$ is a sparse matrix, in which only N_{RF} and M (out of NN_{RF} and NM) elements in each row and column, respectively, are nonzero numbers. Thus, the complexity for computing the Euclidean in (47) is $K\mathcal{O}\left(4MN_{\text{RF}} + M\right)$, which is much higher than the computations in (48)–(51). Furthermore, obtaining $\{\mathbf{W}[k]\}$ with (42) has a complexity of $\mathcal{O}(NKN_{\text{RF}}^2)$. As a result, the total complexity of Algorithm 4 is approximated as $\mathcal{I}_{4,\text{outer}}\mathcal{I}_{4,\text{inner}}K\mathcal{O}\left(4MN_{\text{RF}} + M\right) + \mathcal{I}_{4,\text{outer}}\mathcal{O}(NKN_{\text{RF}}^2)$, where $\mathcal{I}_{4,\text{outer}}$ and $\mathcal{I}_{4,\text{inner}}$ are the numbers of outer and inner iterations until this algorithm converges.

From the above analysis, the total complexity of the proposed JCAS design in Algorithm 1 can be approximated as

$$\begin{aligned}\mathcal{C}_{\text{JCAS-HBF}} &= \mathcal{O}\Big(\mathcal{I}_2N^3K^{3.5}M^{3.5} + 4\mathcal{I}_3N^2JM \\ &\quad + 4\mathcal{I}_{4,\text{outer}}\mathcal{I}_{4,\text{inner}}KMN_{\text{RF}} + \mathcal{I}_{4,\text{outer}}NKN_{\text{RF}}^2\Big),\end{aligned} \tag{54}$$

with the note that $N, K \gg M, N_{\text{RF}}$.

IV. Communications–Sensing Tradeoff and HBF Performance Analysis

In JCAS systems, the joint function of sensing and communications causes performance loss to both subsystems. Since the radar sensing targets and communications MSs are generally located at different locations, a waveform designed for target sensing may not be able to focus the power to communications MSs and mitigate inter-user interference, and vice versa, the

sensing receiver may be misled by a well-designed communications waveform which does not cover the desired sensing angles. The communications–sensing performance tradeoff can be improved by proper settings of set $\mathcal{J}$ and the sensing constraint, as discussed next.

A. Effects of Set $\mathcal{J}$ on JCAS Performance Tradeoff

From (32) and (33), we can write the overall objective of the JCAS design in problem (15) as

$$\gamma = \gamma_{\text{sens}} + \gamma_{\text{comm}}, \tag{55}$$

where $\gamma_{\text{sens}} = \frac{\rho}{J}\sum_{k\in\mathcal{J}} \left\|\mathbf{Q}[k]\mathbf{Q}^{\text{H}}[k] - \bar{\mathbf{R}}[k]\right\|_{\mathcal{F}}^2$ and $\gamma_{\text{comm}} = \frac{\bar{\rho}}{J}\sum_{k\in\mathcal{J}}\|\mathbf{Q}[k] - \hat{\mathbf{Q}}[k]\|_{\mathcal{F}}^2$. The two Frobenius distances measure how the designed beampatterns and precoders are close to the benchmarks, i.e., $\bar{\mathbf{R}}[k]$ and $\hat{\mathbf{Q}}[k]$, respectively. Therefore, they reflect the performance of the radar sensing and communications subsystems. In the following, we analyze the tradeoff between the performance of the two subsystems based on these distance functions.

Note that the communications–sensing performance tradeoff depends on the weighting factors $\{\rho, \bar{\rho}\}$ and on the set of JCAS subcarriers $\mathcal{J}$. Specifically, when ρ is small, a larger set $\mathcal{J}$ should be employed because otherwise, the design objective γ in (15) is dominated by γ_{comm}, which results in the precoders maximizing the performance of the communications rather than sensing accuracy. In contrast, when ρ increases, γ_{sens} has more significant contribution to γ, which improves the sensing accuracy. Note that enlarging $\mathcal{J}$ causes a loss in communications performance because more communications bands are interfered by sensing. However, this only occurs among subcarriers in $\mathcal{J}$.

When a strict sensing accuracy is imposed on the design, i.e., $\rho \to 1$, the communications rate of the proposed JCAS scheme converges to $\sum_{m\in\mathcal{M}}\sum_{k\in\mathcal{K}\setminus\mathcal{J}} r_{mk}$, which is the total rate at communications-only subcarriers. In contrast, that of the conventional JCAS system, i.e., when $\mathcal{J} \equiv \mathcal{K}$, can decrease without bound. This is more clearly seen in the interference-limited regime of the considered MU-MIMO systems, wherein a larger SNR does not ensure communications performance improvement. Therefore, compared to the conventional JCAS design, the proposed scheme with a larger ρ but smaller $\mathcal{J}$ is more beneficial in guaranteeing a good performance tradeoff between the two subsystems, especially in the interference-limited regime. We will further discuss this in Section V.

B. Effects of Set $\mathcal{J}$ on HBF Performance

The size of $\mathcal{J}$ has a significant impact on HBF performance. To see this, we factorize the objective (41) as

$$\eta = \underbrace{\sum_{k\in\mathcal{K}\setminus\mathcal{J}} \left\|\hat{\mathbf{Q}}[k] - \mathbf{F}\mathbf{W}[k]\right\|_{\mathcal{F}}^2}_{\text{communications only}} + \underbrace{\sum_{k\in\mathcal{J}} \left\|\tilde{\mathbf{Q}}[k] - \mathbf{F}\mathbf{W}[k]\right\|_{\mathcal{F}}^2}_{\text{JCAS}}, \tag{56}$$

which follows (17). We recall that in (56), $\hat{\mathbf{Q}}[k], k \in \mathcal{K}\setminus\mathcal{J}$ in the first term is obtained from problem (14) for communications only, while $\tilde{\mathbf{Q}}[k], k \in \mathcal{J}$ in the second term is the solution to the JCAS design in (15).

It is observed from (56) that a larger $\mathcal{J}$ forces $\mathbf{F}\mathbf{W}[k]$ closer to $\tilde{\mathbf{Q}}[k]$ rather than $\hat{\mathbf{Q}}[k]$, which leads to a more significant performance loss of HBF communications systems. In contrast, when $\mathcal{J}$ is small, the objective function η is dominated by the communications part, and hence, $\mathbf{F}\mathbf{W}[k]$ approaches $\hat{\mathbf{Q}}[k]$ while becoming far from $\tilde{\mathbf{Q}}[k]$, leading to poor sensing performance.

The observation that the sensing accuracy can be improved with a stricter sensing constraint, or equivalently, a larger ρ, further motivates employing a smaller set $\mathcal{J}$ but a larger ρ for JCAS-HBF systems. This is similar to the earlier design suggestion in Section IV-A. Despite the similarity, we note that the design suggestion in this subsection is drawn from the objective function η of the HBF design problem (41), and, thus, is only valid for HBF systems and not seen for DBF. As a result, the above analysis unveil a two-fold effect of the JCAS subcarriers set $\mathcal{J}$ on communications–sensing performance tradeoff of wideband JCAS-HBF systems. In particular, when employing a reduced number of JCAS subcarriers, the HBF system has a more significant loss in sensing performance than the DBF one. We will further numerically verify this through simulation results in the next section.

We note that the observation above is not due to the two-step design in (15) and (16). If we consider the combined design

$$\underset{\{\mathbf{Q}[k]\}}{\text{minimize}}\ \bar{\gamma} \triangleq \rho\sum_{k\in\mathcal{J}}\left\|\sum_{m\in\mathcal{M}}\mathbf{F}\mathbf{w}_m[k]\mathbf{w}_m^{\text{H}}[k]\mathbf{F}^{\text{H}} - \bar{\mathbf{R}}[k]\right\|_{\mathcal{F}}^2 + \bar{\rho}\sum_{k\in\mathcal{K}}\sum_{m\in\mathcal{M}}\left\|\mathbf{F}\mathbf{w}_m[k] - \bar{\mathbf{q}}_m[k]\right\|^2, \tag{57a}$$

$$\text{subject to } (10\text{b}), (10\text{c}), \tag{57b}$$

with

$$\bar{\gamma} = \rho\sum_{k\in\mathcal{J}}\left\|\mathbf{F}\mathbf{W}[k]\mathbf{W}^{\text{H}}[k]\mathbf{F}^{\text{H}} - \bar{\mathbf{R}}[k]\right\|_{\mathcal{F}}^2 + \bar{\rho}\sum_{k\in\mathcal{K}\setminus\mathcal{J}}\left\|\mathbf{F}\mathbf{W}[k] - \hat{\mathbf{Q}}[k]\right\|_{\mathcal{F}}^2 + \bar{\rho}\sum_{k\in\mathcal{J}}\left\|\mathbf{F}\mathbf{W}[k] - \hat{\mathbf{Q}}[k]\right\|_{\mathcal{F}}^2, \tag{58}$$

we can still make the same observations as discuss above.

V. Simulation Results

We herein provide numerical results to demonstrate the efficiency of the proposed JCAS design. Unless otherwise stated, we set $N = 32$, $M = 4$, $K = 64$, BW $= 1$ GHz, $f_c = 28$ GHz [72], [73]. The SNR is defined as $P_{\text{BS}}/\sigma_{\text{n}}^2$, where the noise power is normalized and fixed to $\sigma_{\text{n}}^2 = 1$. The channel realizations are generated based on (2) with $\phi_p \sim \mathcal{U}[0°, 360°)$, $\alpha_p \sim \mathcal{CN}(0, 1)$, and $\tau_p \sim \mathcal{U}[0, \tau_{\max}]$, where $\tau_{\max} = 20$ ns is the maximum delay [74]. Furthermore, we assume $P = 4$ for the number of propagation paths due to the limited scattering in high-frequency systems [52], [75]. Unless otherwise stated, the sensing targets are assumed to be located at angles

$\boldsymbol{\Theta}_{\rm d} \in \{-60^\circ, -30^\circ, 30^\circ, 60^\circ\}$, and the corresponding desired beampattern is defined as [54]

$$\mathcal{P}_{\rm d}(\theta_t, f_k) = \begin{cases} 1, & \theta_t \in [\theta_{\rm d} - \delta_\theta, \theta_{\rm d} + \delta_\theta] \\ 0, & \text{otherwise} \end{cases}, \quad \forall k, \tag{59}$$

where $\delta_\theta = 5$ is the half of the mainlobes of $\mathcal{P}_{\rm d}(\theta_t, f_k)$. We use the modeling toolbox YALMIP with solver MOSEK to solve the convex subproblem (29), whereas, subproblems (34) and (46) are solved with the Manopt toolbox [76]. The convergence tolerances of Algorithms 2 and 4 are both set to $\varepsilon = 10^{-3}$.

A. Convergence of Algorithms 2 and 4

First, we show the convergence improvement of Algorithms 2 and 4 based on the proposed initialization in Fig. 2 with $N = 32$, $M = 4$, $N_{\rm RF} = 6$, $K = 64$, $\rho = 0.4$, $J = K/2$, and SNR $= 10$ dB. We recall that Algorithm 2 maximizes the sum rate $\frac{1}{K}\sum_{k\in\mathcal{K}}\sum_{m\in\mathcal{M}}\tilde{r}_{mk}$ in 14, while Algorithm 4 minimizes the Frobenius distance $\sum_{k\in\mathcal{K}}\sum_{m\in\mathcal{M}}\|\bar{\mathbf{q}}_m[k] - \mathbf{F}\mathbf{w}_m[k]\|^2$ in (16). It is observed that the objective values of both algorithms converge well, but their convergence is significantly affected by the initial points. Specifically, Algorithm 2 initialized with water-filling-ZF solution converges after about only four iterations, while the random initialization requires more than 14 iterations. In Algorithm 4, the proposed initialization method also offers a significantly faster convergence with a slightly lower objective value compared to the random one and the solution in [70] based on all frequencies, i.e., $[\bar{\mathbf{Q}}[1], \ldots, \bar{\mathbf{Q}}[K]]$. As a result, these proposed initial solutions lead to a remarkable complexity reduction of the overall design in Algorithm 1. It is also seen for both algorithms that these initializations already have relatively good performance.

B. Performance of the Proposed JCAS Scheme

Next, we evaluate the performance of the proposed JCAS design by investigating its resultant beampatterns and communications rates. As discussed earlier, the proposed scheme applies to both the designs of DBF and HBF transceivers. Thus, we investigate both beamforming architectures. For comparisons, we consider the following schemes: (i) the proposed JCAS design ("Prop. JCAS"); the conventional JCAS system wherein the communications and sensing subsystems operate at (ii) overlapping (see Fig. 1(a)) [9], [54], [55], [56], [57], [61], [62] and (iii) non-overlapping subcarriers (see Fig. 1(b)) [61], [62], [63], [64], [65], [66], [67] ("Conv. JCAS, overlap" and "Conv. JCAS, non-overlap", respectively); and (iv) the communications-only system ("Communication only"). In the non-overlapping JCAS system, we assume that the first J subcarriers are employed for sensing, and the remaining are dedicated to communications. Note from Algorithm 1 that for the communications-only system, our designs coincide with the SCA and Reimannian manifold optimization approaches, which are well-known frameworks for sum-rate maximization in MU-MIMO systems [77] and HBF designs [41], respectively. Thus, the achievable rate in the communications-only system is not only the upper bound

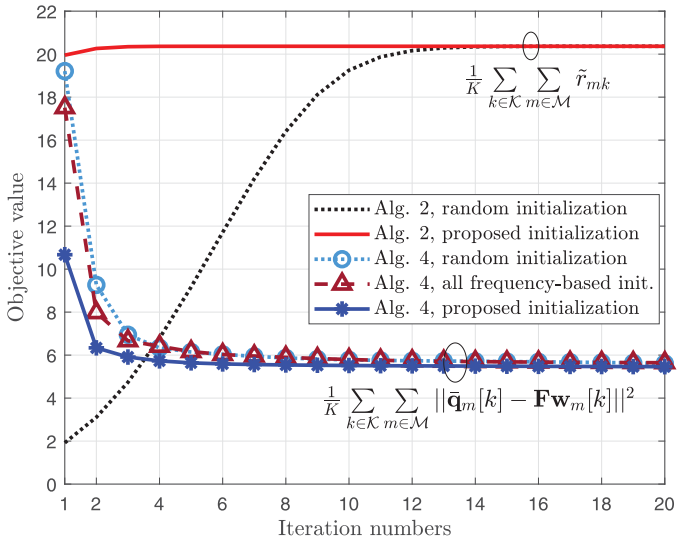

Fig. 2. Convergence of Algorithms 2 and 4, with $N = 32$, $M = 4$, $N_{\rm RF} = 6$, $K = 64$, $\rho = 0.4$, $J = K/2$, and SNR $= 10$ dB.

of the communications rate but also the benchmark for the proposed beamforming design for the consider JCAS system.

In Fig. 3, we plot the normalized beampatterns of the proposed and conventional JCAS schemes. We consider $N = 32$, $N_{\rm RF} = 6$, $M = 4$, $K = 64$, $\rho = \{0.2, 0.4\}$ and $J = K/2 = 32$. As expected, increasing ρ yields improved beampatterns with higher peaks at desired detection angles $\theta_t \in \boldsymbol{\Theta}_{\rm d}$ and lower peaks at $\theta_t \notin \boldsymbol{\Theta}_{\rm d}$, implying more reliable radar sensing systems. In particular, despite the reduced number of JCAS subcarriers, the proposed JCAS design still forms good beampatterns, which exhibit only very small gaps with respect to the ones obtained by the conventional design with overlapping subcarriers, especially for DBF in Fig. 3(a). For the case of HBF in Fig. 3(b), the beampatterns formed by the proposed JCAS-HBF scheme are slightly worse with lower peaks compared with the conventional overlapping design. However, they still point to accurate detection angles $\boldsymbol{\Theta}_{\rm d}$ with high main lobes and low side lobes outside $\boldsymbol{\Theta}_{\rm d}$. More specifically, for moderate ρ, the peak-to-side lobe ratios (PSLRs) of the proposed JCAS-HBF design are just slightly lower than those of the conventional overlapping design, as seen in Table I for $\rho = 0.4$. The comparisons of beampatterns and their corresponding PSLRs in Fig. 3 and Table I further support the conclusion in Section IV-B that the reduced number of JCAS subcarriers can significantly affect the sensing performance in JCAS-HBF systems, and this can be overcome by employing a larger ρ. Further quantified evaluations of the beampatterns based on the average mean square errors (MSEs) will be presented in Section V-C. The results in Fig. 3 and Table I show that as expected, using non-overlapping subcarriers for the communications and sensing functions yields the best sensing beampatterns. However, this comes at the cost of limited communications performance, as shown next.

In Fig. 4, we show the communications sum rates of the proposed JCAS designs with DBF and HBF transceivers. We assume the same simulation parameters as in Fig. 3 to guarantee that communications performance is compared under similar beampatterns. From Fig. 4, we observe:

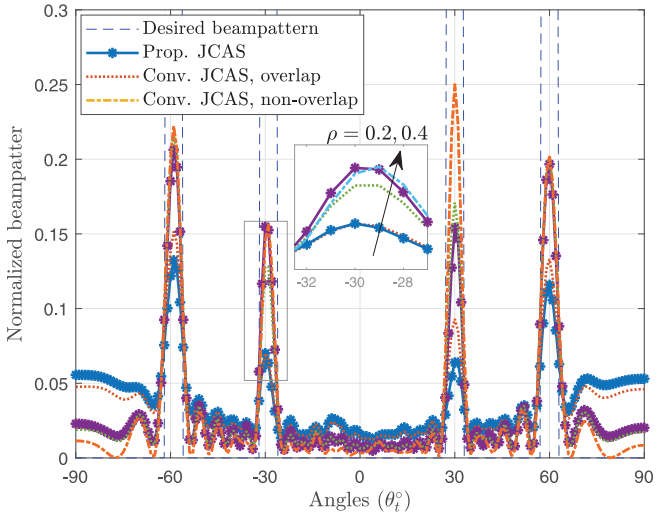

(a) DBF

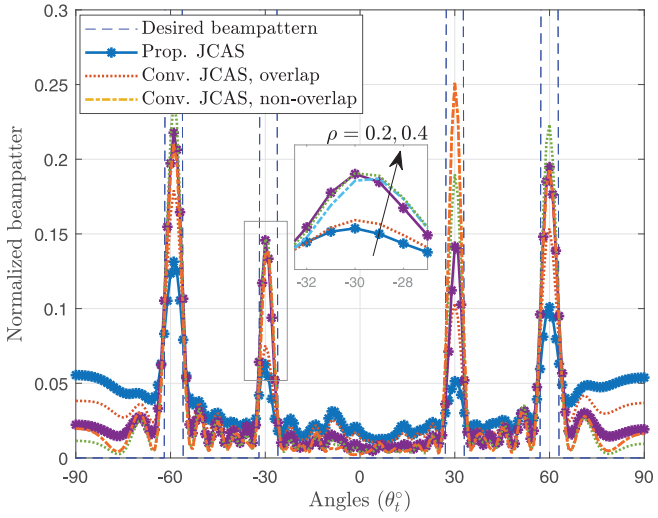

(b) HBF

Fig. 3. Beampatterns of the proposed JCAS design for DBF and HBF architectures with $N = 32$, $N_{\text{RF}} = 6$, $M = 4$, $K = 64$, $\rho = \{0.2, 0.4, 0.6\}$, $J = K/2$, and SNR $= 12$ dB. (a) DBF. (b) HBF.

TABLE I
PSLRs OF THE CONVENTIONAL AND PROPOSED JCAS SCHEMES IN DBF AND HBF SYSTEMS WITH $N = 32$, $N_{\text{RF}} = 6$, $M = 4$, $K = 64$, $\rho = \{0.2, 0.4, 0.6\}$, $J = K/2$, AND SNR $= 12$ DB

Architecture	JCAS schemes	$\rho = 0.2$	$\rho = 0.4$
DBF	Prop. JCAS	1.76 dB	6.92 dB
	Conv. JCAS, overlap	3.61 dB	7.01 dB
	Conv. JCAS, non-overlap	8.26 dB	
HBF	Prop. JCAS	1.38 dB	6.81 dB
	Conv. JCAS, overlap	4.91 dB	7.55 dB
	Conv. JCAS, non-overlap	8.30 dB	

- The JCAS systems have considerable performance degradation with respect to the communications-only systems, especially in the interference-limited regime, as clearly seen at high SNRs in both figures. Furthermore, the loss is more significant when ρ becomes larger. Indeed, the JCAS waveform needs to simultaneously serve both communications MSs and radar targets. Hence, its capability to mitigate inter-user interference (IUI) is significantly reduced, making the communications subsystem vulnerable and having degraded achievable rates in an interference-limited regime or when using a larger ρ. We note that such a performance degradation at high SNRs is not seen in IUI-free scenarios such as single-user systems [78].
- It is worth noting that the severe IUI discussed above only occurs within JCAS subcarriers. Thus, for both DBF and HBF, it is reasonable to observe that the performance loss of the conventional overlapping JCAS system is much more severe than the proposed setting. Regarding the conventional non-overlapping counterpart, the impact of sensing on communications performance depends on the beamforming architectures. Specifically, with DBF, the beamformers are completely frequency-dependent, and thus, they can be designed dedicated for

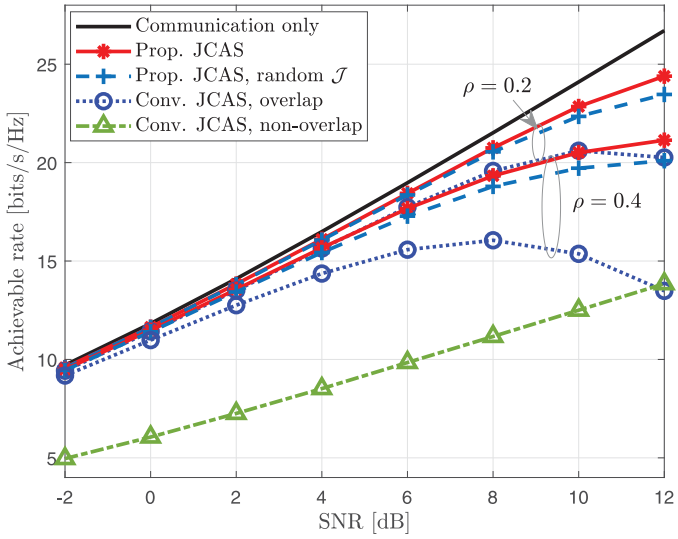

(a) DBF

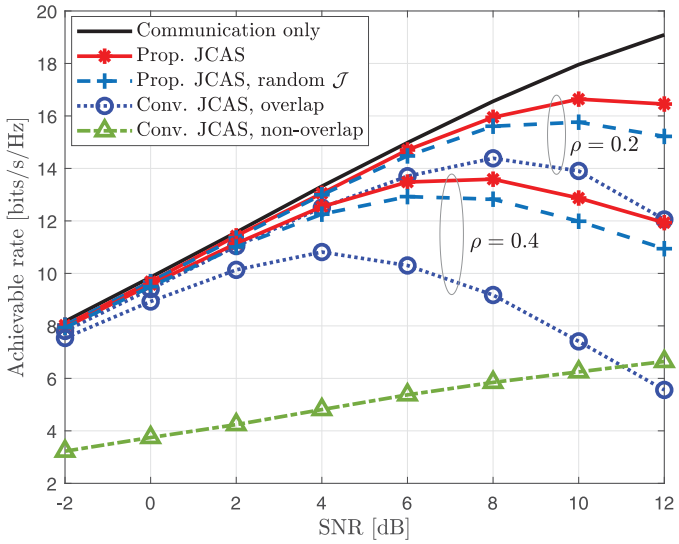

(b) HBF

Fig. 4. Communications performance of the proposed JCAS design for DBF and HBF with $N = 32$, $N_{\text{RF}} = 6$, $M = 4$, $K = 64$, $\rho = \{0.2, 0.4\}$, and $J = K/2$. (a) DBF. (b) HBF.

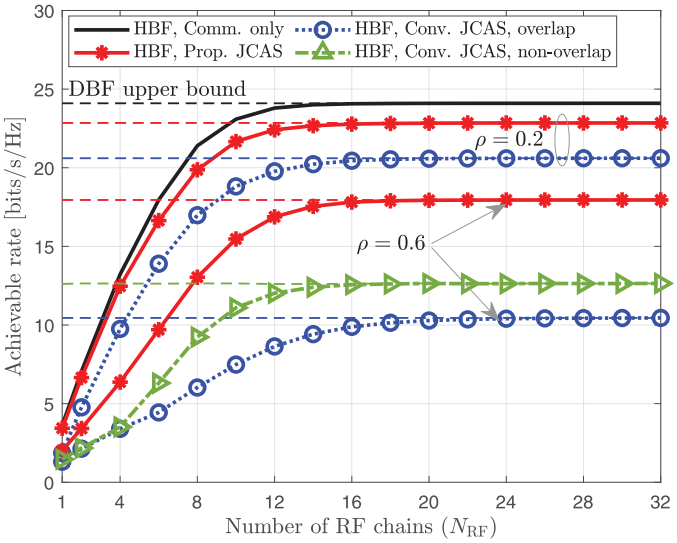

Fig. 5. Communications rates of the proposed JCAS design with $N = 32$, $N_{\mathrm{RF}} = \{1, 2, \ldots, N\}$, $M = 4$, $K = 64$, $\rho = \{0.2, 0.6\}$, $J = K/2$, and SNR $= 10$ dB.

sensing or communications at the corresponding subcarriers. Furthermore, as we assume $J = K/2$, i.e., each subsystem uses a half of the bandwidth, the achievable rate of the non-overlapping JCAS-DBF scheme is approximately equal to $r_{\mathrm{com}}/2$, where r_{com} is the achievable rate of the communication-only system. However, this approximation is not valid for HBF because the analog precoder is frequency-flat and common for the dual functions. This explains the low achievable rate of the non-overlapping JCAS-HBF scheme in Fig. 4(b).

- Although the proposed method does not guarantee to avoid the decreasing communications rate in an interference-limited regime, it ensures that the rate has a non-decreasing lower bound: $\sum_{k\in\mathcal{K}} r_k \geq r_{\mathrm{LB}} \triangleq \sum_{k\in\mathcal{K}\setminus\mathcal{J}} r_k$, where $r_k \triangleq \sum_{m\in\mathcal{M}} r_{mk}$. This follows the fact that r_{LB} is not affected by the radar subsystem. In contrast, that of the conventional system decreases without bounds as the IUI and/or ρ increases. This analysis agrees with the observations in Fig. 4 that while the rate of conventional systems quickly decreases at moderate-to-high SNRs, those of the proposed schemes keep increasing in Fig. 4(a) and just slightly decrease in Fig. 4(b).
- Compared to the case of communications-only, the performance loss of the HBF in Fig. 4(b) is more significant than that of the DBF in Fig. 4(a), which settles with the discussion in Section IV-B. Furthermore, the proposed subcarrier selection strategy offers better performance than the random one. The gains are more clearly seen with a larger ρ.

In Fig. 5, we compare the communications performance of the proposed JCAS-HBF design with those of the conventional JCAS-HBF and the communications-only HBF systems for various N_{RF} and ρ. We set $N = 32$, $N_{\mathrm{RF}} = \{1, 2, \ldots, N\}$, $M = 4$, $K = 64$, $\rho = \{0.2, 0.6\}$, $J = 32$, and SNR $= 10$ dB. We also show the DBF performance as the upper bound of HBF in this figure. It is observed for both the communications-only and JCAS systems that the HBF sum rates increase with N_{RF} and essentially reach the DBF performance when N_{RF} becomes sufficiently large. However, the increasing rate of the HBF sum rates also depends on the JCAS design. Specifically, considering the case $\rho = 0.6$, the proposed JCAS-HBF design has a rapidly increasing sum rate and realizes the DBF systems with $N_{\mathrm{RF}} = 16$ RF chains, whereas $N_{\mathrm{RF}} = 20$ RF chains are required by the conventional overlapping JCAS-HBF design. It is also clearly seen in this case that the proposed JCAS-HBF scheme with only $N_{\mathrm{RF}} = 8$ RF chains performs better than the conventional overlapping JCAS system with both the HBF and DBF architectures. Indeed, with $\rho = 0.6$, the overall objective in (15a) is easily dominated by the sensing objective in the first term. This limits the contribution of the communications objective over JCAS subcarriers $\mathcal{J}$, causing a loss in the total rate. With $\mathcal{J} \equiv \mathcal{K}$ as in the conventional overlapping JCAS design, this loss occurs over the entire bandwidth, leading to poor communications performance even in DBF systems, as analyzed in Section IV-A. The loss becomes more serious in HBF architectures with limited RF chains due to the two-fold effect of $\mathcal{J} \equiv \mathcal{K}$ on overlapping JCAS-HBF systems, as analyzed in Section IV-B. Furthermore, due to the reduced bands employed for communications, the non-overlapping JCAS with DBF and HBF is outperformed by the proposed JCAS-HBF scheme with only $N_{\mathrm{RF}} = 8$ RF chains when $\rho = 0.6$. In the next figures, we will show that the high communications performance gains of the proposed JCAS scheme are achieved with only marginal loss in the sensing beampattern MSEs, compared with the conventional JCAS designs.

C. Communications–Sensing Performance Tradeoff

Next, we demonstrate superior communications–sensing performance tradeoff of the proposed JCAS scheme through investigating the sum rate and MSEs of the beampatterns versus J in Fig. 6. We consider $N = 32$, $N_{\mathrm{RF}} = 6$, $M = 4$, $K = 64$, $\rho = \{0.2, 0.4, 0.6, 0.8\}$, $J = [1, 8, 16, \ldots, K]$, and SNR $= 12$ dB. The beampattern MSE is defined as $\mathrm{MSE} = \frac{1}{JT}\sum_{k\in\mathcal{J}}\sum_{t=1}^{T} |\mathcal{P}_{\mathrm{d}}(\theta_t, f_k) - \mathbf{a}^{\mathsf{H}}(\theta_t, f_k)\mathbf{R}[k]\mathbf{a}(\theta_t, f_k)|^2$. It is observed for the proposed JCAS scheme that increasing J leads to decreasing rates and MSEs, implying the communications performance loss but improved sensing accuracy. The same is also observed for the conventional non-overlapping JCAS design which employs J and $K - J$ dedicated sensing and communications subcarriers, respectively. Furthermore, as expected, the rates and MSEs of the communications-only and conventional overlapping JCAS systems are constant with J, and they serve as the lower and upper bounds on the rates and MSEs, respectively, of the proposed scheme. Indeed, the proposed JCAS design coincides with the communications-only case as $J \to 0$ and the conventional JCAS case as $J \to K$. The conventional non-overlapping subcarrier allocation offers reliable sensing beampatterns with low MSEs (Fig. 6b), but it cannot ensure satisfactory communications performance (Fig. 6a). As J and ρ are sufficiently large, the gaps between the MSEs of the proposed and conventional overlapping and non-overlapping schemes become marginal, while their rate improvements are still significant. For example, with $J = 40$

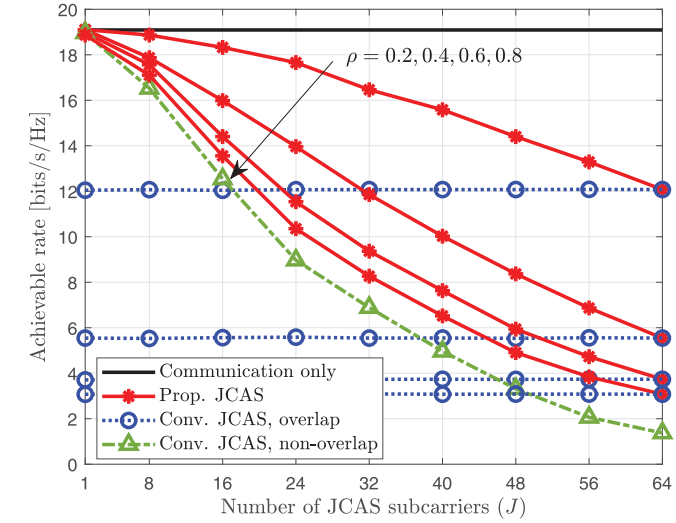

(a) Communications performance

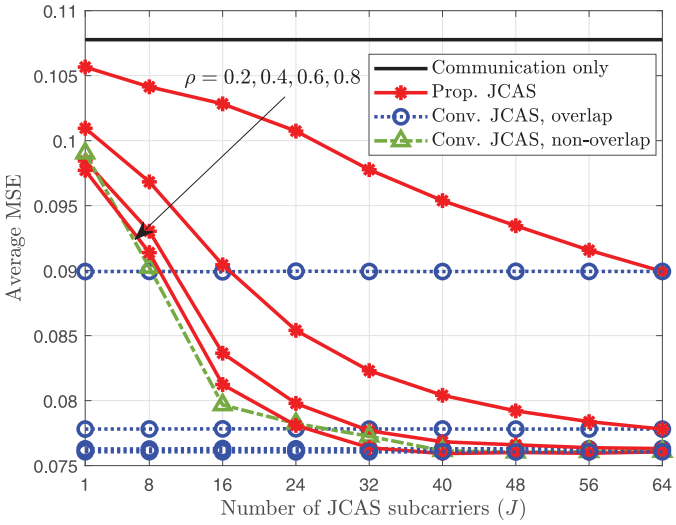

(b) Sensing beampattern MSEs

Fig. 6. Communications rates and MSEs of the proposed JCAS design with $N = 32$, $N_{\text{RF}} = 6$, $M = 4$, $K = 64$, $\rho = \{0.2, 0.4, 0.6\}$, $J = [1, 8, 16, \ldots, K]$, and SNR $= 12$ dB. (a) Communications performance. (b) Sensing beampattern MSEs.

and $\rho = 0.6$, the proposed JCAS design achieves 104.39% and 59.62% higher communications rates with similar sensing beampattern MSEs as the conventional overlapping and non-overlapping counterparts, respectively. Furthermore, with $\rho = 0.8$, the sensing function in the proposed JCAS design performs similar to that in the non-overlapping counterpart, but with better communications performance. This indicates on the potential for improved communication–sensing performance tradeoff, as specified next.

In Fig. 7, we plot the sum rates versus the beampatten MSEs based on the results in Fig. 6, with the same simulation parameters. It is observed for each ρ that, the rates and MSEs of the conventional overlapping JCAS system always serve as the lower and upper bounds on the communications and sensing performance, respectively, of the proposed scheme. Furthermore, it is reasonable to see that these bounds are attained by the proposed scheme when $J = K$. An important observation is that for the

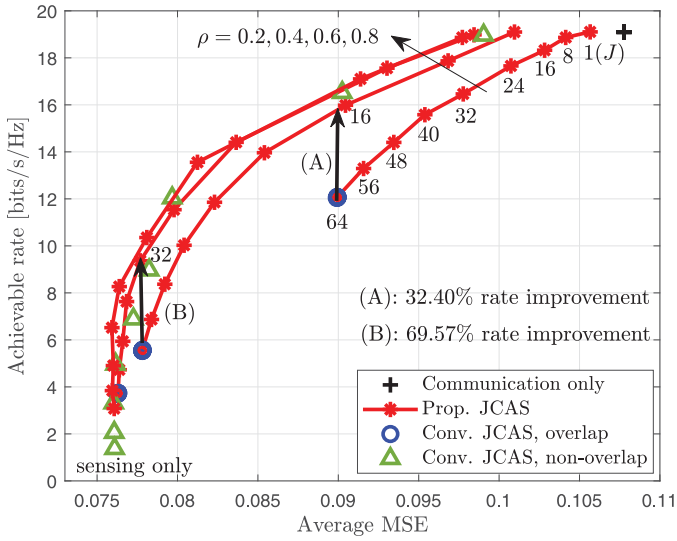

Fig. 7. Communications–sensing performance tradeoff of the proposed JCAS design with $N = 32$, $M = 4$, $N_{\text{RF}} = 6$, $K = 64$, $\rho = \{0.2, 0.4, 0.6\}$, $J = [1, 8, 16, \ldots, K]$, and SNR $= 12$ dB.

same MSE, the proposed JCAS scheme can always achieve a much larger sum rate by employing a larger ρ but smaller J (as suggested in Section IV), which clearly justify the improvement in the system communications–sensing performance tradeoff as the motivation of the proposed JCAS design. For example, to guarantee an MSE of 9×10^{-2} of the conventional system with $\rho = 0.2$, we can apply the proposed scheme with $\{\rho, J\} = \{0.4, 16\}$ and attain 32.40% higher sum rate (please see arrow (A)). Similarly, an MSE of 7.7×10^{-2} can be achieved with 69.57% improvement in communications rate by the proposed scheme with $\{\rho, J\} = \{0.6, 32\}$ instead of using the conventional one with $\{\rho, J\} = \{0.4, K\}$ (arrow (B)). Similar to the observation in Fig. 6, the improved communications–sensing performance tradeoff of the proposed scheme achieves with respect to the conventional non-overlapping JCAS design is seen for large ρ and J, i.e., for $\rho = \{0.6, 0.8\}$ and $J \geq 32$.

D. Performance of the Proposed JCAS Design With Various Numbers of Targets and CSI Errors

In the previous simulations, we have fixed the number of targets to four and their angles to $\{\pm 30°, \pm 60°\}$. To further demonstrate the efficiency of the proposed scheme, we show in Figs. 8 and 9 its sensing beampatterns, communications rates, and average beampattern MSEs for various numbers of sensing targets and angles. Specifically, we consider $\{1, 3, 5, 7\}$ targets at angles $\{0°\}$, $\{0°, \pm 60°\}$, $\{0°, \pm 30°, \pm 60°\}$, and $\{0°, \pm 30°, \pm 45°, \pm 60°\}$, respectively. The other simulation parameters are set similar to those in Figs. 3 and 4, i.e., $N = 32$, $N_{\text{RF}} = 6$, $M = 4$, $K = 64$, $\rho = 0.4$, $J = K/2$, and SNR $= 12$ dB.

It is seen Figs. 8 and 9 that the proposed scheme still perform well as for the case of 4 targets considered in Figs. 3–7. Specifically, in Fig. 8, it generates highly reliable beampatterns covering the desired targets for all the considered numbers and distributions of the targets. In particular, it achieves the best communications performance with only slightly higher sensing

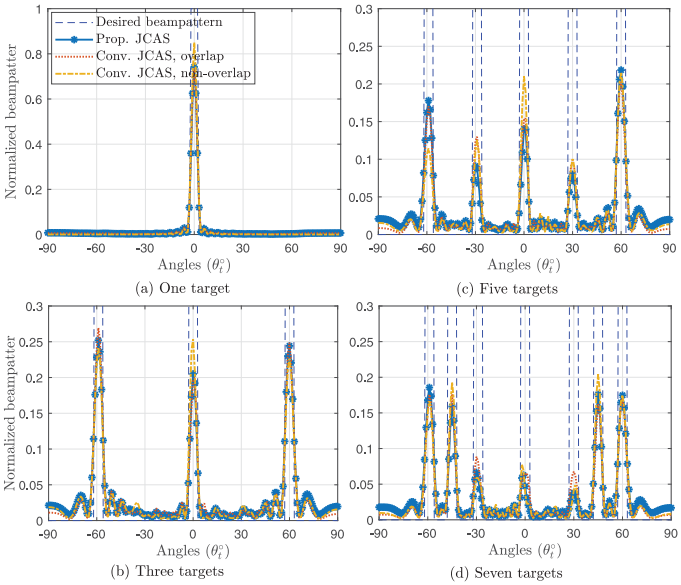

Fig. 8. Beampatterns of the proposed JCAS-HBF design for sensing targets at angles (a) $\{0^\circ\}$, (b) $\{0^\circ, \pm 60^\circ\}$, (c) $\{0^\circ, \pm 30^\circ, \pm 60^\circ\}$, and (d) $\{0^\circ, \pm 30^\circ, \pm 45^\circ, \pm 60^\circ\}$ with $N = 32$, $N_{\text{RF}} = 6$, $M = 4$, $K = 64$, $\rho = 0.4$, $J = K/2$, and SNR $= 12$ dB.

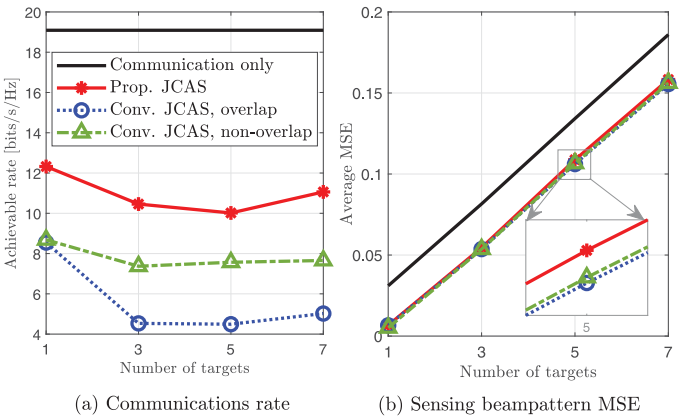

Fig. 9. Communications rates and MSEs of the proposed JCAS-HBF design for $\{1, 3, 5, 7\}$ sensing targets with $N = 32$, $N_{\text{RF}} = 6$, $M = 4$, $K = 64$, $\rho = 0.4$, $J = K/2$, and SNR $= 12$ dB. (a) Communications rate. (b) Sensing beampattern MSE.

beampattern MSEs compared to the conventional JCAS designs with overlapping and non-overlapping subcarrier allocation. As expected, all the compared schemes have increased sensing beampattern MSEs and decreased communications rates as there are more targets. However, when covering a large number of targets, the BS has a higher chance to cover the communications MSs to improve the system sum rate, as seen for seven targets in Fig. 9(a).

Finally, we examine the performance of the considered JCAS-HBF systems under imperfect CSI. We denote by $\hat{\mathbf{h}}_{mk}$ the imperfect channel estimates of $\mathbf{h}_{mk}$. It can be modeled as $\hat{\mathbf{h}}_{mk} = \mathbf{h}_{mk} - \tilde{\mathbf{h}}_{mk}$, where $\tilde{\mathbf{h}}_{mk}$ represents the CSI error with entries following the distribution $\mathcal{CN}(0, \epsilon_{mk}^2)$. Here, ϵ_{mk} is the CSI uncertainty level of $\hat{\mathbf{h}}_{mk}$. In Fig. 10, we show the communications rates and sensing beampattern MSEs of the considered schemes versus $\epsilon_{mk} = \epsilon = \{0, 0.1, \ldots, 1\}, \forall m, k$.

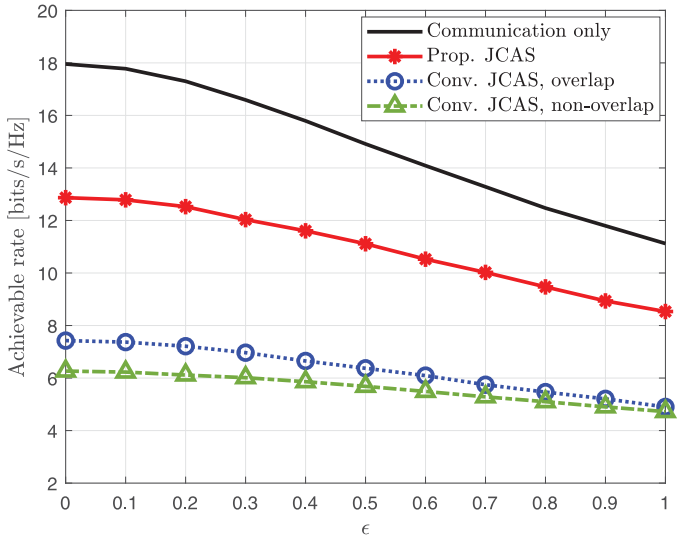

Fig. 10. Communications rates under CSI errors of the proposed JCAS-HBF design with $N = 32$, $M = 4$, $N_{\text{RF}} = 6$, $K = 64$, $\rho = 0.4$, $J = K/2$, SNR $= 10$ dB, and $\epsilon = \{0, 0.1, \ldots, 1\}$.

For $\epsilon = 0$, the channel is perfectly estimated. It is observed that as ϵ increases, the performance of all the considered systems decreases, however, at different speeds. Specifically, the communications-only system has the most significant performance loss because it requires the CSI at all the subcarriers for the HBF design. In the proposed JCAS system, $K - J$ dedicated subcarriers are used for communications, while the remaining J subcarriers are used for both communications and sensing. Thus, its achievable rate also decreases relatively fast with ϵ. The two other conventional JCAS systems are less affected by the CSI error as smaller factions of subcarriers are used for communications. However, even at $\epsilon = 1$, the proposed JCAS design still outperforms the conventional ones. On the other hand, because the CSI is not required for the beampattern design, it does not affect the sensing performance.

VI. Conclusion

We studied wideband MU-MIMO JCAS systems with HBF transceiver architectures. Aiming at maximizing the communications rate while ensuring sensing accuracy, we proposed an efficient JCAS design with a new subcarrier allocation strategy. Specifically, we proposed to use a subset of subcarriers for radar sensing, while enabling communications over all the available subcarriers. The beamforming design for JCAS was conducted leveraging the SCA and Riemannian manifold optimization approaches. Our numerical results showed that reliable sensing accuracy, or more specifically, low MSEs and high PSLRs of the sensing beampatterns, could still be achieved with a reduced number of JCAS subcarriers, while the performance of the communications was dramatically improved. In particular, both the analysis and simulations suggested that a reduced number of JCAS subcarriers and a stricter sensing constraint should be employed for a better communications-sensing performance tradeoff. Utilization of the beam squint effect to improve the performance of ultra-wideband THz JCAS-HBF systems is a potential extension of this work.

REFERENCES

[1] M. Giordani, M. Polese, M. Mezzavilla, S. Rangan, and M. Zorzi, "Toward 6G networks: Use cases and technologies," *IEEE Commun. Mag.*, vol. 58, no. 3, pp. 55–61, Mar. 2020.

[2] K. V. Mishra, M. B. Shankar, V. Koivunen, B. Ottersten, and S. A. Vorobyov, "Toward millimeter-wave joint radar communications: A signal processing perspective," *IEEE Signal Process. Mag.*, vol. 36, no. 5, pp. 100–114, Sep. 2019.

[3] T. S. Rappaport et al., "Wireless communications and applications above 100 GHz: Opportunities and challenges for 6G and beyond," *IEEE Access*, vol. 7, pp. 78729–78757, 2019.

[4] N. T. Nguyen et al., "Beam squint effects in THz communications with UPA and ULA: Comparison and hybrid beamforming design," in *Proc. IEEE Global Commun. Conf. Workshop*, 2022, pp. 1754–1759.

[5] Q. Zhang, X. Wang, Z. Li, and Z. Wei, "Design and performance evaluation of joint sensing and communication integrated system for 5G mmWave enabled CAVs," *IEEE J. Sel. Topics Signal Process.*, vol. 15, no. 6, pp. 1500–1514, Nov. 2021.

[6] I. Gresham et al., "Ultra-wideband radar sensors for short-range vehicular applications," *IEEE Trans. Microw. Theory Techn.*, vol. 52, no. 9, pp. 2105–2122, Sep. 2004.

[7] J. A. Zhang et al., "An overview of signal processing techniques for joint communication and radar sensing," *IEEE J. Sel. Topics Signal Process.*, vol. 15, no. 6, pp. 1295–1315, Nov. 2021.

[8] A. Hassanien, M. G. Amin, Y. D. Zhang, and F. Ahmad, "Signaling strategies for dual-function radar communications: An overview," *IEEE Aerosp. Electron. Syst. Mag.*, vol. 31, no. 10, pp. 36–45, Oct. 2016.

[9] J. A. Zhang, X. Huang, Y. J. Guo, J. Yuan, and R. W. Heath, "Multibeam for joint communication and radar sensing using steerable analog antenna arrays," *IEEE Trans. Veh. Technol.*, vol. 68, no. 1, pp. 671–685, Jan. 2018.

[10] C. Ouyang, Y. Liu, and H. Yang, "Performance of downlink and uplink integrated sensing and communications (ISAC) systems," *IEEE Wireless Commun. Lett.*, vol. 11, no. 9, pp. 1850–1854, Sep. 2022.

[11] F. Liu et al., "Integrated sensing and communications: Towards dual-functional wireless networks for 6G and beyond," *IEEE J. Sel. Areas Commun.*, vol. 40, no. 6, pp. 1728–1767, Jun. 2022.

[12] D. Ma, N. Shlezinger, T. Huang, Y. Liu, and Y. C. Eldar, "Joint radar-communication strategies for autonomous vehicles: Combining two key automotive technologies," *IEEE Signal Process. Mag.*, vol. 37, no. 4, pp. 85–97, Jul. 2020.

[13] T. Huang, N. Shlezinger, X. Xu, Y. Liu, and Y. C. Eldar, "MAJoRCom: A dual-function radar communication system using index modulation," *IEEE Trans. Signal Process.*, vol. 68, pp. 3423–3438, 2020.

[14] D. Ma et al., "Spatial modulation for joint radar-communications systems: Design, analysis, and hardware prototype," *IEEE Trans. Veh. Technol.*, vol. 70, no. 3, pp. 2283–2298, Mar. 2021.

[15] D. Ma, N. Shlezinger, T. Huang, Y. Liu, and Y. C. Eldar, "FRaC: FMCW-based joint radar-communications system via index modulation," *IEEE J. Sel. Topics Signal Process.*, vol. 15, no. 6, pp. 1348–1364, Nov. 2021.

[16] A. Hassanien, M. G. Amin, Y. D. Zhang, and F. Ahmad, "Dual-function radar-communications: Information embedding using sidelobe control and waveform diversity," *IEEE Trans. Signal Process.*, vol. 64, no. 8, pp. 2168–2181, Apr. 2016.

[17] P. Kumari, J. Choi, N. González-Prelcic, and R. W. Heath, "IEEE 802.11ad-based radar: An approach to joint vehicular communication-radar system," *IEEE Trans. Veh. Technol.*, vol. 67, no. 4, pp. 3012–3027, Apr. 2018.

[18] A. R. Chiriyath, B. Paul, and D. W. Bliss, "Radar-communications convergence: Coexistence, cooperation, and co-design," *IEEE Trans. Cogn. Commun. Netw.*, vol. 3, no. 1, pp. 1–12, Mar. 2017.

[19] L. Zheng, M. Lops, Y. C. Eldar, and X. Wang, "Radar and communication coexistence: An overview: A review of recent methods," *IEEE Signal Process. Mag.*, vol. 36, no. 5, pp. 85–99, Sep. 2019.

[20] B. Li, A. P. Petropulu, and W. Trappe, "Optimum co-design for spectrum sharing between matrix completion based MIMO radars and a MIMO communication system," *IEEE Trans. Signal Process.*, vol. 64, no. 17, pp. 4562–4575, Sep. 2016.

[21] A. F. Martone, K. A. Gallagher, and K. D. Sherbondy, "Joint radar and communication system optimization for spectrum sharing," in *Proc. IEEE Radar Conf.*, 2019, pp. 1–6.

[22] F. Liu, C. Masouros, A. Li, H. Sun, and L. Hanzo, "MU-MIMO communications with MIMO radar: From co-existence to joint transmission," *IEEE Trans. Wireless Commun.*, vol. 17, no. 4, pp. 2755–2770, Apr. 2018.

[23] F. Liu, C. Masouros, A. Li, and T. Ratnarajah, "Robust MIMO beamforming for cellular and radar coexistence," *IEEE Trans. Wireless Commun.*, vol. 6, no. 3, pp. 374–377, Jun. 2017.

[24] X. Liu, T. Huang, Y. Liu, and Y. C. Eldar, "Transmit beamforming with fixed covariance for integrated MIMO radar and multiuser communications," in *Proc. IEEE Int. Conf. Acoust. Speech Signal Process.*, 2022, pp. 8732–8736.

[25] J. Pritzker, J. Ward, and Y. C. Eldar, "Transmit precoder design approaches for dual-function radar-communication systems," 2022, *arXiv:2203.09571*.

[26] X. Liu, T. Huang, N. Shlezinger, Y. Liu, J. Zhou, and Y. C. Eldar, "Joint transmit beamforming for multiuser MIMO communications and MIMO radar," *IEEE Trans. Signal Process.*, vol. 68, pp. 3929–3944, 2020.

[27] J. Pritzker, J. Ward, and Y. C. Eldar, "Transmit precoding for dual-function radar-communication systems," in *Proc. Annu. Asilomar Conf. Signals Syst. Comput.*, 2021, pp. 1065–1070.

[28] X. Fang, W. Feng, Y. Chen, N. Ge, and Y. Zhang, "Joint communication and sensing: Models and potentials of using MIMO," 2022, *arXiv:2205.09409*.

[29] J. Johnston, L. Venturino, E. Grossi, M. Lops, and X. Wang, "MIMO OFDM dual-function radar-communication under error rate and beampattern constraints," *IEEE J. Sel. Areas Commun.*, vol. 40, no. 6, pp. 1951–1964, Jun. 2022.

[30] K. Wu, J. A. Zhang, X. Huang, Y. J. Guo, and R. W. Heath, "Waveform design and accurate channel estimation for frequency-hopping MIMO radar-based communications," *IEEE Trans. Commun.*, vol. 69, no. 2, pp. 1244–1258, Feb. 2021.

[31] X. Tong et al., "Environment sensing considering the occlusion effect: A multi-view approach," *IEEE Trans. Signal Process.*, vol. 70, pp. 3598–3615, 2022.

[32] F. Liu, L. Zhou, C. Masouros, A. Li, W. Luo, and A. Petropulu, "Toward dual-functional radar-communication systems: Optimal waveform design," *IEEE Trans. Signal Process.*, vol. 66, no. 16, pp. 4264–4279, Aug. 2018.

[33] B. Tang and P. Stoica, "MIMO multifunction RF systems: Detection performance and waveform design," *IEEE Trans. Signal Process.*, vol. 70, pp. 4381–4394, 2022.

[34] W. Wu, B. Tang, and X. Wang, "Constant-modulus waveform design for dual-function radar-communication systems in the presence of clutter," *IEEE Trans. Aerosp. Electron. Syst.*, vol. 59, no. 4, pp. 4005–4017, Aug. 2023.

[35] R. Liu, M. Li, Q. Liu, and A. L. Swindlehurst, "Dual-functional radar-communication waveform design: A symbol-level precoding approach," *IEEE J. Sel. Topics Signal Process.*, vol. 15, no. 6, pp. 1316–1331, Nov. 2021.

[36] R. Liu, M. Li, Q. Liu, and A. L. Swindlehurst, "Joint waveform and filter designs for STAP-SLP-based MIMO-DFRC systems," *IEEE J. Sel. Areas Commun.*, vol. 40, no. 6, pp. 1918–1931, Jun. 2022.

[37] K. Wu, J. A. Zhang, Z. Ni, X. Huang, Y. J. Guo, and S. Chen, "Joint communications and sensing employing optimized MIMO-OFDM signals," 2022, *arXiv:2208.09791*.

[38] M. Temiz, E. Alsusa, and M. W. Baidas, "A dual-function massive MIMO uplink OFDM communication and radar architecture," *IEEE Trans. Cogn. Commun. Netw.*, vol. 8, no. 2, pp. 750–762, Jun. 2022.

[39] S. Buzzi, C. D'Andrea, and M. Lops, "Using massive MIMO arrays for joint communication and sensing," in *Proc. Annu. Asilomar Conf. Signals Syst. Comput.*, 2019, pp. 5–9.

[40] M. F. Keskin, H. Wymeersch, and V. Koivunen, "MIMO-OFDM joint radar-communications: Is ICI friend or foe?" *IEEE J. Sel. Topics Signal Process.*, vol. 15, no. 6, pp. 1393–1408, Nov. 2021.

[41] X. Yu, J.-C. Shen, J. Zhang, and K. B. Letaief, "Alternating minimization algorithms for hybrid precoding in millimeter wave MIMO systems," *IEEE J. Sel. Topics Signal Process.*, vol. 10, no. 3, pp. 485–500, Apr. 2016.

[42] F. Sohrabi and W. Yu, "Hybrid digital and analog beamforming design for large-scale antenna arrays," *IEEE J. Sel. Topics Signal Process.*, vol. 10, no. 3, pp. 501–513, Apr. 2016.

[43] N. T. Nguyen and K. Lee, "Unequally sub-connected architecture for hybrid beamforming in massive MIMO systems," *IEEE Trans. Wireless Commun.*, vol. 19, no. 2, pp. 1127–1140, Feb. 2020.

[44] N. T. Nguyen, K. Lee, and H. Dai, "Hybrid beamforming and adaptive RF chain activation for uplink cell-free millimeter-wave massive MIMO systems," *IEEE Trans. Veh. Technol.*, vol. 71, no. 8, pp. 8739–8755, Aug. 2022.

[45] N. T. Nguyen, M. Ma, N. Shlezinger, Y. C. Eldar, A. L. Swindlehurst, and M. Juntti, "Deep unfolding-enabled hybrid beamforming design for mmWave massive MIMO systems," in *Proc. IEEE Int. Conf. Acoust. Speech Signal Process.*, 2023, pp. 1–5.
[46] F. Liu and C. Masouros, "Hybrid beamforming with sub-arrayed MIMO radar: Enabling joint sensing and communication at mmWave band," in *Proc. IEEE Int. Conf. Acoust. Speech Signal Process.*, 2019, pp. 7770–7774.
[47] Z. Cheng, Z. He, and B. Liao, "Hybrid beamforming for multi-carrier dual-function radar-communication system," *IEEE Trans. Cogn. Commun. Netw.*, vol. 7, no. 3, pp. 1002–1015, Sep. 2021.
[48] C. Qi, W. Ci, J. Zhang, and X. You, "Hybrid beamforming for millimeter wave MIMO integrated sensing and communications," *IEEE Commun. Lett.*, vol. 26, no. 5, pp. 1136–1140, May 2022.
[49] M. A. Islam, G. C. Alexandropoulos, and B. Smida, "Integrated sensing and communication with millimeter wave full duplex hybrid beamforming," in *Proc. IEEE Int. Conf. Commun.*, 2022, pp. 4673–4678.
[50] X. Wang, Z. Fei, J. A. Zhang, and J. Xu, "Partially-connected hybrid beamforming design for integrated sensing and communication systems," *IEEE Trans. Commun.*, vol. 70, no. 10, pp. 6648–6660, Oct. 2022.
[51] N. Shlezinger, M. Ma, O. Lavi, N. T. Nguyen, Y. C. Eldar, and M. Juntti, "AI-empowered hybrid MIMO beamforming," 2023, *arXiv:2303.01723*.
[52] N. T. Nguyen et al., "Deep unfolding hybrid beamforming designs for THz massive MIMO systems," 2023, *arXiv:2302.12041*.
[53] M. Ma, N. T. Nguyen, and M. Juntti, "Beam squint analysis and mitigation via hybrid beamforming design in THz communications," 2023, *arXiv:2303.12466*.
[54] Z. Cheng, Z. He, and B. Liao, "Hybrid beamforming design for OFDM dual-function radar-communication system," *IEEE J. Sel. Topics Signal Process.*, vol. 15, no. 6, pp. 1455–1467, Nov. 2021.
[55] A. M. Elbir, K. V. Mishra, and S. Chatzinotas, "Terahertz-band joint ultra-massive MIMO radar-communications: Model-based and model-free hybrid beamforming," *IEEE J. Sel. Topics Signal Process.*, vol. 15, no. 6, pp. 1468–1483, Nov. 2021.
[56] S. D. Liyanaarachchi, C. B. Barneto, T. Riihonen, M. Heino, and M. Valkama, "Joint multi-user communication and MIMO radar through full-duplex hybrid beamforming," in *Proc. IEEE Int. Online Symp. Joint Commun. Sens. (JC&S)*, 2021, pp. 1–5.
[57] C. B. Barneto, T. Riihonen, S. D. Liyanaarachchi, M. Heino, N. González-Prelcic, and M. Valkama, "Beamformer design and optimization for full-duplex joint communication and sensing at mm-waves," 2021, *arXiv:2109.05932*.
[58] X. Qiang, L. You, C. G. Tsinos, W. Wang, X. Gao, and B. Ottersten, "Joint communications and sensing for hybrid massive MIMO LEO satellite systems with beam squint," in *Proc. IEEE Int. Conf. Commun. Workshop*, 2022, pp. 963–968.
[59] K. Wu, J. A. Zhang, X. Huang, R. W. Heath, and Y. J. Guo, "Green joint communications and sensing employing analog multi-beam antenna arrays," *IEEE Commun. Mag.*, vol. 61, no. 7, pp. 172–178, Jul. 2023.
[60] F. Gao, L. Xu, and S. Ma, "Integrated sensing and communications with joint beam-squint and beam-split for mmWave/THz massive MIMO," *IEEE Trans. Commun.*, vol. 71, no. 5, pp. 2963–2976, May 2023.
[61] F. Wang, H. Li, and M. A. Govoni, "Power allocation and co-design of multicarrier communication and radar systems for spectral coexistence," vol. 67, no. 14, pp. 3818–3831, Jul. 2019.
[62] T. Tian, T. Zhang, G. Li, and T. Zhou, "Mutual information-based power allocation and co-design for multicarrier radar and communication systems in coexistence," *IEEE Access*, vol. 7, pp. 159300–159312, 2019.
[63] M. Bică and V. Koivunen, "Multicarrier radar-communications waveform design for RF convergence and coexistence," in *Proc. IEEE Int. Conf. Acoust. Speech Signal Process.*, 2019, pp. 7780–7784.
[64] S. D. Liyanaarachchi, C. B. Barneto, T. Riihonen, and M. Valkama, "Joint OFDM waveform design for communications and sensing convergence," in *Proc. IEEE Int. Conf. Commun.*, 2020, pp. 1–6.
[65] C. Shi, F. Wang, S. Salous, and J. Zhou, "Joint subcarrier assignment and power allocation strategy for integrated radar and communications system based on power minimization," *IEEE Sensors J.,* vol. 19, no. 23, pp. 11167–11179, Dec. 2019.
[66] C. Shi, Y. Wang, F. Wang, S. Salous, and J. Zhou, "Joint optimization scheme for subcarrier selection and power allocation in multicarrier dual-function radar-communication system," *IEEE Syst. J.*, vol. 15, no. 1, pp. 947–958, Mar. 2021.
[67] A. Ahmed, Y. D. Zhang, A. Hassanien, and B. Himed, "OFDM-based joint radar-communication system: Optimal sub-carrier allocation and power distribution by exploiting mutual information," in *Proc. Annu. Asilomar Conf. Signals Syst. Comput.*, 2019, pp. 559–563.
[68] D. R. Fuhrmann and G. San Antonio, "Transmit beamforming for MIMO radar systems using signal cross-correlation," *IEEE Trans. Aerosp. Electron. Syst.*, vol. 44, no. 1, pp. 171–186, Jan. 2008.
[69] H. Hojatian, J. Nadal, J.-F. Frigon, and F. Leduc-Primeau, "Flexible unsupervised learning for massive MIMO subarray hybrid beamforming," in *Proc. IEEE Global Commun. Conf.*, 2022, pp. 3833–3838.
[70] H. Yuan, J. An, N. Yang, K. Yang, and T. Q. Duong, "Low complexity hybrid precoding for multiuser millimeter wave systems over frequency selective channels," *IEEE Trans. Veh. Technol.*, vol. 68, no. 1, pp. 983–987, Jan. 2019.
[71] W. Rudin et al., *Principles of Mathematical Analysis*, vol. 3. New York, NY, USA: McGraw-Hill, 1976.
[72] "3GPP Specification series," TS 38 series. [Online]. Available: http://www.3gpp.org/DynaReport/38-series.htm
[73] "Study on channel model for frequencies from 0.5 to 100 GHz," 3rd Generation Partnership Project (3GPP), ETSI TR 138 900 36.331, Dec. 2019, v16.1.0, release 16.
[74] Y. Chen, Y. Xiong, D. Chen, T. Jiang, S. X. Ng, and L. Hanzo, "Hybrid precoding for wideband millimeter wave MIMO systems in the face of beam squint," *IEEE Trans. Wireless Commun.*, vol. 20, no. 3, pp. 1847–1860, Mar. 2021.
[75] L. Dai, J. Tan, Z. Chen, and H. V. Poor, "Delay-phase precoding for wideband THz massive MIMO," *IEEE Trans. Wireless Commun.*, vol. 21, no. 9, pp. 7271–7286, Sep. 2022.
[76] N. Boumal, B. Mishra, P.-A. Absil, and R. Sepulchre, "Manopt, a Matlab toolbox for optimization on manifolds," *J. Mach. Learn. Res.*, vol. 15, no. 42, pp. 1455–1459, 2014.
[77] L.-N. Tran, M. F. Hanif, A. Tolli, and M. Juntti, "Fast converging algorithm for weighted sum rate maximization in multicell MISO downlink," *IEEE Signal Process. Lett.*, vol. 19, no. 12, pp. 872–875, Dec. 2012.
[78] N. T. Nguyen, N. Shlezinger, K.-H. Ngo, V.-D. Nguyen, and M. Juntti, "Joint communications and sensing design for multi-carrier MIMO systems," in *Proc. IEEE Work. Statist. Signal Process.*, 2023. [Online]. Available: https://arxiv.org/pdf/2306.14006.pdf

Nhan Thanh Nguyen (Member, IEEE) received the B.S. degree in electronics and telecommunications engineering from Hanoi University of Science and Technology, Hanoi, Vietnam, in 2014, and the M.S. and Ph.D. degrees in electrical and information engineering from the Seoul National University of Science and Technology, Seoul, South Korea, in 2017 and 2020, respectively. From October 2019 to March 2020, he was a Visiting Researcher with North Carolina State University, Raleigh, NC, USA. Since September 2020, he has been a Postdoctoral Researcher with the Centre for Wireless Communications, University of Oulu, Finland. In 2022, he was a Visiting Scholar with the Ben-Gurion University of the Negev and the Weizmann Institute of Science, Israel. His research interests include signal processing, optimization, and applied machine learning for wireless communications. He was the recipient of the Best M.S. Thesis Award (2017), Best Ph.D. Dissertation Award (2020), Best Paper Awards at the International Conference on Advanced Technologies for Communications (ATC, 2021) and at the IEEE Statistical Signal Processing Workshop (SSP, 2023), Nokia Foundation Award (2022), and Academy of Finland Fellowship (2023).

Nir Shlezinger (Senior Member, IEEE) received the B.Sc., M.Sc., and Ph.D. degrees in electrical and computer engineering from Ben-Gurion University, Israel, in 2011, 2013, and 2017, respectively. He is an Assistant Professor with the School of Electrical and Computer Engineering, Ben-Gurion University, Israel. From 2017 to 2019, he was a Postdoctoral Researcher with the Technion, and from 2019 to 2020, he was a Postdoctoral Researcher with the Weizmann Institute of Science, where he was awarded the FGS prize for outstanding research achievements. His research interests include communications, information theory, signal processing, and machine learning.

Yonina C. Eldar (Fellow, IEEE) received the B.Sc. degree in physics, in 1995, and the B.Sc. degree in electrical engineering, in 1996, from Tel-Aviv University (TAU), Tel-Aviv, Israel, and the Ph.D. degree in electrical engineering and computer science, in 2002, from the Massachusetts Institute of Technology (MIT), Cambridge, MA, USA. She is currently a Professor with the Department of Mathematics and Computer Science, Weizmann Institute of Science, Rehovot, Israel, where she holds the Dorothy and Patrick Gorman Professorial Chair and the Heads of the Center for Biomedical Engineering. She was previously a Professor with the Department of Electrical Engineering at the Technion, where she held the Edwards Chair in engineering. She is also a Visiting Professor at MIT, a Visiting Scientist at Broad Institute, a Visiting Research Collaborator at Princeton, an Adjunct Professor at Duke University, an Advisory Professor at Fudan University, a Distinguished Visiting Professor at Tsinghua University, and a Visiting Professor at Stanford. She is a member of the Israel Academy of Sciences and Humanities (elected in 2017) and the Academia Europaea (elected in 2023), a EURASIP Fellow, a fellow of the Asia-Pacific Artificial Intelligence Association, and a fellow of the 8400 Health Network. Her research interests are in the broad areas of statistical signal processing, sampling theory and compressed sensing, learning and optimization methods, and their applications to biology, medical imaging, and optics. She received many awards for excellence in research and teaching, including the IEEE Signal Processing Society Technical Achievement Award (2013), the IEEE/AESS Fred Nathanson Memorial Radar Award (2014), and the IEEE Kiyo Tomiyasu Award (2016). She was a Horev Fellow of the Leaders in Science and Technology program at the Technion and an Alon Fellow. She received the Michael Bruno Memorial Award from the Rothschild Foundation, the Weizmann Prize for Exact Sciences, the Wolf Foundation Krill Prize for Excellence in Scientific Research, the Henry Taub Prize for Excellence in Research (twice), the Hershel Rich Innovation Award (three times), the Award for Women with Distinguished Contributions, the Andre and Bella Meyer Lectureship, the Career Development Chair at the Technion, the Muriel & David Jacknow Award for Excellence in Teaching, and the Technion's Award for Excellence in Teaching (two times). She received several best paper awards and best demo awards together with her research students and colleagues including the SIAM outstanding Paper Prize, the UFFC Outstanding Paper Award, the Signal Processing Society Best Paper Award and the IET Circuits, Devices and Systems Premium Award, was selected as one of the 50 most influential women in Israel and in Asia, and is a highly cited researcher. She was a member of the Young Israel Academy of Science and Humanities and the Israel Committee for Higher Education. She is the Editor in Chief of *Foundations and Trends in Signal Processing*, a member of the IEEE Sensor Array and Multichannel Technical Committee and serves on several other IEEE committees. In the past, she was a Signal Processing Society Distinguished Lecturer, member of the IEEE Signal Processing Theory and Methods and Bio Imaging Signal Processing technical committees, and served as an Associate Editor for the IEEE TRANSACTIONS ON SIGNAL PROCESSING, the *EURASIP Journal of Signal Processing*, the *SIAM Journal on Matrix Analysis and Applications*, and the *SIAM Journal on Imaging Sciences*. She was Co-Chair and Technical Co-Chair of several international conferences and workshops. She is the author of the book "Sampling Theory: Beyond Bandlimited Systems" and co-author of seven other books.

Markku Juntti (Fellow, IEEE) received the M.Sc. (EE) and D.Sc. (EE) degrees from the University of Oulu, Oulu, Finland, in 1993 and 1997, respectively. He was with the University of Oulu from 1992 to 1998. From 1994 to 1995, he was a Visiting Scholar with Rice University, Houston, TX, USA. From 1999 to 2000, he was a Senior Specialist with Nokia Networks, Oulu, Finland. Since 2000, he has been a Professor in communications engineering with the Centre for Wireless Communications (CWC), University of Oulu, where he leads the Communications Signal Processing (CSP) Research Group. He also serves as the Head of CWC – Radio Technologies (RT) Research Unit. His research interests include signal processing for wireless networks as well as communication and information theory. He is an Author or Co-Author of almost 500 papers published in international journals and conference records as well as in books *Wideband CDMA for UMTS* in 2000–2010, *Handbook of Signal Processing Systems* in 2013 and 2018, and *5G Wireless Technologies*, in 2017. He is also an Adjunct Professor with the Department of Electrical and Computer Engineering, Rice University, Houston, TX, USA. He is an Editor of the IEEE TRANSACTIONS ON WIRELESS COMMUNICATIONS, and served previously in similar role in the IEEE TRANSACTIONS ON COMMUNICATIONS and the IEEE TRANSACTIONS ON VEHICULAR TECHNOLOGY. He was Secretary of the IEEE Communication Society Finland Chapter in 1996–1997 and the Chair for years 2000–2001. He has been a Secretary of the Technical Program Committee (TPC) of the 2001 IEEE International Conference on Communications (ICC), and the Chair or Co-Chair of the Technical Program Committee of several conferences including the 2006 and 2021 IEEE International Symposium on Personal, Indoor and Mobile Radio Communications (PIMRC), the Signal Processing for Communications Symposium of IEEE Globecom 2014, the Symposium on Transceivers and Signal Processing for 5G Wireless and mm-Wave Systems of IEEE GlobalSIP 2016, the ACM NanoCom 2018, the 2019 International Symposium on Wireless Communication Systems (ISWCS), and the 2024 IEEE International Symposium on Joint Communications & Sensing (JC&S). He has also served as the General Chair of 2011 IEEE Communication Theory Workshop (CTW 2011) and 2022 IEEE Workshop on Signal Processing Advances in Wireless Communications (SPAWC).